CHALMERS
UNIVERSITY OF TECHNOLOGY

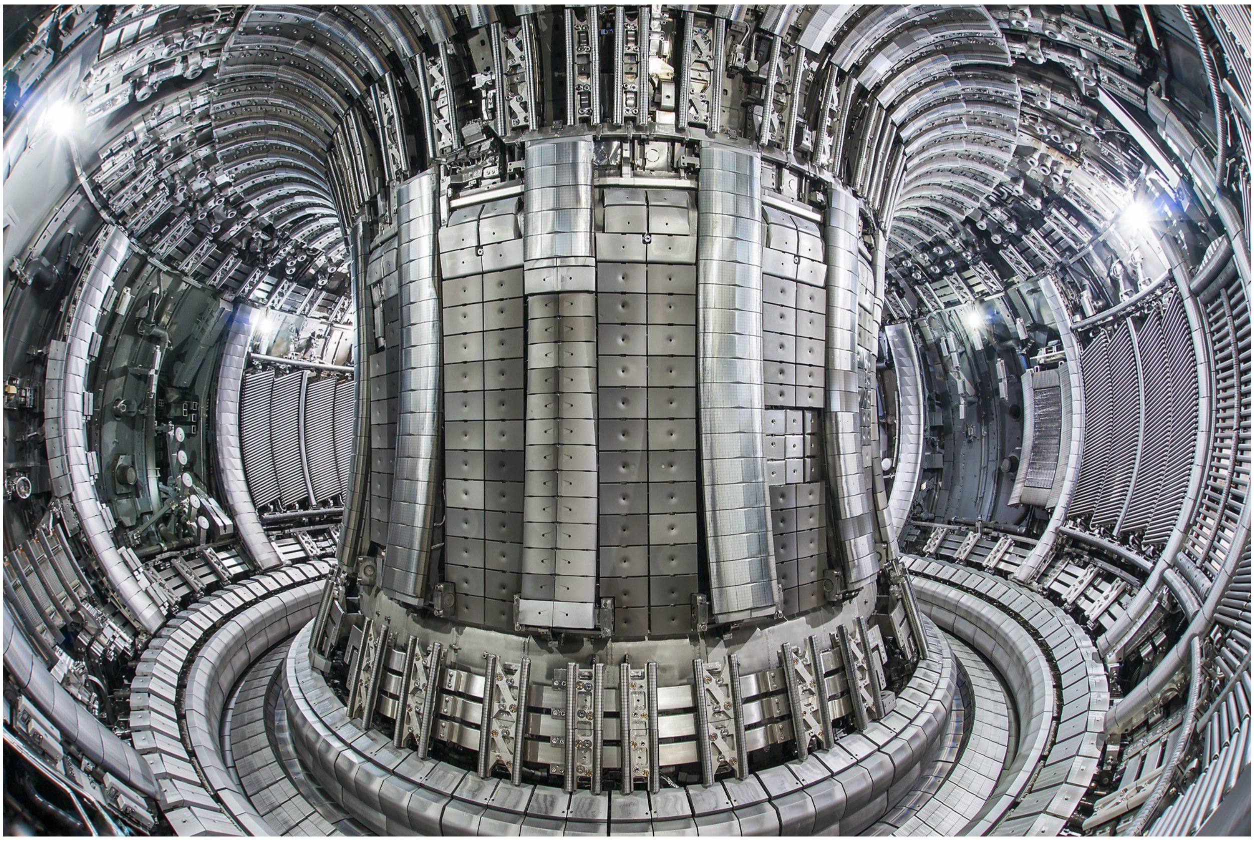

Sensitivities of the runaway current in JET disruptions to massive gas injection and initial plasma current

Thesis for the degree of Master of Science in Physics

CHRISTIAN GUSTAVSSON

DEPARTMENT OF PHYSICS
CHALMERS UNIVERSITY OF TECHNOLOGY
Gothenburg, Sweden 2024
www.chalmers.se

Master's thesis 2024

Sensitivities of the runaway current in JET disruptions to massive gas injection and initial plasma current

CHRISTIAN GUSTAVSSON

Department of Physics
Division of Subatomic, High Energy and Plasma Physics
Plasma Theory Research Group
Chalmers University of Technology
Gothenburg, Sweden 2024

Sensitivities of the runaway current in JET disruptions to massive gas injection and initial plasma current
CHRISTIAN GUSTAVSSON

© CHRISTIAN GUSTAVSSON, 2024.

Supervisors:	Mathias Hoppe, Department of Electrical Engineering, KTH Ida Ekmark, Department of Physics, Chalmers
Examiner:	István Pusztai, Department of Physics, Chalmers

Master's Thesis 2024
Chalmers University of Technology
Department of Physics
Division of Subatomic, High Energy and Plasma Physics
Plasma Theory Research Group
SE-412 96 Gothenburg
Telephone +46 31 772 1000

Cover: An internal view of the Joint European Torus vessel with a complete metallic wall of beryllium and tungsten. Image credit: EUROfusion, *JET vessel internal view*, licensed under CC BY 4.0

Typeset in LaTeX
Gothenburg, Sweden 2024

Sensitivities of the runaway current in JET disruptions to massive gas injection and initial plasma current
CHRISTIAN GUSTAVSSON
Department of Physics
Chalmers University of Technology

Abstract

The Joint European Torus (JET) tokamak, located at the Culham Centre for Fusion Energy in the UK, has been a leader in magnetic confinement fusion (MCF) research for decades. As the world's largest operational tokamak until 2023, JET has significantly advanced the understanding and technology needed for controlled fusion energy, which aims to provide a clean, large-scale energy source by replicating the processes that power the Sun. A primary challenge in tokamak operation is managing plasma disruptions, which can terminate plasma confinement and generate runaway electrons (REs). These high-energy electrons can damage reactor components, thus studying REs is vital for the viability of fusion energy. As the fusion community progresses towards advanced reactors like ITER in France and SPARC in the USA, understanding and controlling REs becomes even more important.

This study uses the Disruption Runaway Electron Analysis Model (DREAM) to investigate the conditions under which REs form during tokamak disruptions. The main objective of this thesis is to model the conditions for the existence of REs in JET massive gas injection (MGI) discharges, focusing on their dependence on magnetic field strength, initial plasma current, as well as the ratio of injected argon to deuterium. Furthermore, we are interested in how much current is carried by the REs after a disruption. The analysis is conducted through a series of parameter scans using the simulation tool DREAM. Our simulation results show that the RE current is influenced by the initial plasma current and the ratio of injected argon to deuterium, with only a very weak dependence on magnetic field strength. Moreover, our findings suggest that the injection profile of argon significantly affects the parametric trends of the maximum RE current. A uniform injection profile yields an inverted current trend compared to an edge-peaked injection profile, where the latter yields results that are more in line with experimental results.

Keywords: fusion plasma, runaway electron, massive material injection, massive gas injection, disruption mitigation, JET

Acknowledgements

I would like to express my gratitude to the Plasma Theory Group for allowing me to conduct my master's thesis within the group. Everyone here has been very kind and supportive, making this a truly enriching and developmental experience. I am particularly grateful to my supervisors, Mathias and Ida, and to my examiner, István Pusztai, for their keen interest in my work and unwavering support. They have provided invaluable guidance throughout this thesis, always taking the time to answer my questions and offering assistance with any issues related to DREAM, programming, and other aspects of my work. Additionally, they have engaged in insightful discussions about plasma physics with me. Moreover, I appreciate their thorough review of the thesis and valuable suggestions for improvement, which have greatly enhanced the quality of this thesis.

Christian Gustavsson, Gothenburg, June 2024

List of Acronyms

Below is the list of acronyms that have been used throughout this thesis listed in alphabetical order:

CQ	Current Quench
D-T	Deuterium-Tritium
DREAM	Disruption Runaway Electron Analysis Model
ICF	Inertial Confinement Fusion
JET	Joint European Torus
JET-C	Joint European Torus with Carbon wall
JET-ILW	Joint European Torus with ITER-like Wall
LIDAR	Light Detection and Ranging
MCF	Magnetic Confinement Fusion
MGI	Massive Gas Injection
MMI	Massive Material Injection
RE	Runaway Electron
SPI	Shattered Pellet Injection
STEP	Spherical Tokamak for Energy Production
TQ	Thermal Quench
ITER	International Thermonuclear Experimental Reactor

Nomenclature

Below is the nomenclature of parameters and variables that have been used throughout this thesis.

Parameters

I_p	Plasma current [MA]
I_RE	Runaway current [MA]
I_Ω	Ohmic current [MA]
B	Magnetic field strength [T]
T_e	Electron temperature [eV]
n_e	Electron density [m^{-3}]
t_TQ	Thermal quench duration [s]
t_CQ	Current quench duration [s]
$\delta B/B$	Normalized magnetic perturbation amplitude [dimensionless]
f_i	Assimilation fraction [dimensionless]
G_Ar, G_D	Injected gas amounts for argon and deuterium [Pa m^3]
n_Ar, n_D	Ion densities for argon and deuterium [m^{-3}]
R, a	Major and minor radii of the tokamak [m]
b	Wall radius of the tokamak [m]
E	Electric field strength [V/m]
V_p	Plasma volume [m^3]
σ	Electrical conductivity [S/m]

Contents

List of Acronyms ix

Nomenclature xi

List of Figures xv

List of Tables xvii

1 Introduction 1
- 1.1 Purpose . . . 3
- 1.2 Outline . . . 4

2 Plasma and tokamak theory 5
- 2.1 What is plasma physics? . . . 5
- 2.2 The basics of plasma physics . . . 6
- 2.3 Magnetic confinement in a tokamak . . . 7
- 2.4 A theoretical description of plasmas . . . 8
  - 2.4.1 Kinetic theory . . . 9
  - 2.4.2 Collisions and conductivity . . . 11
  - 2.4.3 Electron runaway . . . 12
- 2.5 Runaway generation mechanisms . . . 13
  - 2.5.1 Primary generation mechanisms . . . 14
  - 2.5.2 Secondary generation mechanism . . . 14
- 2.6 Tokamak disruptions . . . 15
  - 2.6.1 The three phases of a disruption . . . 15
  - 2.6.2 Miscellaneous . . . 16
- 2.7 Disruption mitigation . . . 17
  - 2.7.1 Massive material injection (MMI) . . . 17
  - 2.7.2 Assimilation of the injected material . . . 17

3 Simulation framework: DREAM 19
- 3.1 Electron populations and plasma models . . . 19
- 3.2 Ions . . . 21
- 3.3 Poloidal magnetic flux . . . 21
- 3.4 Magnetic geometry, time stepper and numerical solver . . . 22
- 3.5 Radial heat transport . . . 22
- 3.6 Synchrotron losses . . . 23

4 Method 25
4.1 Experimental data 25
4.1.1 Runaway electron existence domain map 26
4.1.2 Plasma current evolution data 26
4.2 Modelling disruptions in DREAM 28
4.2.1 Initialization simulation 29
4.2.2 TQ and CQ simulations 29

5 Results and discussion 31
5.1 Magnetic perturbation strength versus assimilation fraction parameter scans 31
5.2 Plasma current evolution matching 33
5.2.1 Setup 34
5.2.2 Matching 34
5.3 Uniform Ar injection profile 36
5.3.1 Magnetic field strength versus Ar fraction parameter scan . . 36
5.3.2 Initial plasma current versus Ar fraction parameter scan . . . 38
5.4 Edge-peaked Ar injection profile 41
5.4.1 Magnetic field strength versus Ar fraction parameter scan . . 42
5.4.2 Initial plasma current versus Ar fraction parameter scan . . . 42

6 Conclusions 47
6.1 Outlook 48
6.2 Final thoughts 49

Bibliography 51

List of Figures

1.1 Illustration of a tokamak, showing the plasma current (red arrows within the purple plasma) and the magnetic field components: the toroidal field (green arrows parallel to the red arrows), the poloidal field (green arrows orthogonal to the red arrows) and the helical field (black arrows). Image from: Max Planck Institute for Plasma Physics, Germany. 2

2.1 Illustration of the tokamak cross-section showing the toroidal and poloidal magnetic fields, which create helical magnetic field lines around the plasma, forming flux surfaces. Source: (Vallhagen, 2023). 8

2.2 Illustration of the typical behaviour of the electron temperature T_e, induced electric field $E_\|$, plasma current I_p, Ohmic current I_Ω, and runaway current I_RE during a disruption. Source: (Hoppe, 2021). . . 16

3.1 Electron populations as modelled in DREAM. 20

4.1 Runaway electron existence domain map as a function of toroidal field and argon fraction in the disruption mitigation valve. As an example, an Ar fraction = 0.6 means that 60% of the injected material is argon and 40% is deuterium. Each data point corresponds to a unique discharge, but note that in our work we only used data for six of the displayed discharges. The domain entry points and boundaries are provided for JET-C and JET-ILW. The size of the circles represents the maximum runaway current achieved during a disruption. Source: (Reux et al., 2015). 27

4.2 Plasma current evolution for each of the six used discharges. Note that the time axis is only relative, and serves mainly to give an understanding of the time interval for a disruption. What happens before the TQ is related to the startup of a disruption experiment in JET. . 27

5.1 Figures displaying $I_{\mathrm{RE,\,max}}$ as a function of $\delta B/B$ and assimilation fraction (f_i) for four different transport window (TQ) durations t_TQ, using JET discharge #85943 as a baseline discharge. 32

5.2 Plasma current I_p from experimental measurements and simulation during the CQ phase and the beginning of the runaway plateau. The figure also illustrates the simulated Ohmic current I_Ω and RE current I_RE. 35

5.3 $I_{\mathrm{RE,\,max}}$ as a function of baseline magnetic field strength $B = 3$ T scaled by C_B and Ar fraction. Note that the plasma current is not re-scaled consistently with B. 37

5.4 $I_{\mathrm{RE,\,max}}$ as a function of the initial plasma current scale factor C_{I_p} and Ar fraction for the uniform argon injection profile. 39

5.5 (Left) RE current density j_{RE} 2 ms after the onset of the TQ. (Right) Energy density $W_{\mathrm{cold}} + E_{\mathrm{k},\,f_{\mathrm{hot}}}$ at the plasma centre. 40

5.6 RE generation rates at the plasma centre for case A (left) and case B (right). 40

5.7 (Left) Free electron density n_{free} at the plasma centre. (Right) Electric field ratio $E/E_{\mathrm{c,\,eff}}$ at the onset of the CQ (0.2 ms after the onset of the TQ). 40

5.8 Edge-peaked radial profile (equation (5.1)). 41

5.9 $I_{\mathrm{RE,\,max}}$ as a function of baseline magnetic field strength $B = 3$ T scaled by C_B and Ar fraction using the edge-peaked argon injection profile. Note that the initial plasma current is not re-scaled consistently with B. 43

5.10 $I_{\mathrm{RE,\,max}}$ as a function of initial plasma current scale factor C_{I_p} and Ar fraction using the edge-peaked argon injection profile. Note that the magnetic field strength is not re-scaled consistently with $I_{\mathrm{p},0}$. 43

5.11 Free electron density n_{free} at radius $r = 0.8$ m. 44

5.12 Energy density at the plasma centre (left) and $E/E_{\mathrm{c,\,eff}}$ at $r = 0.8$ m (right). 45

5.13 RE generation rates for the cases: Ar fraction $= 0.3$ (left) and Ar fraction $= 0.9$ (right) at radius $r = 0.8$ m. 46

List of Tables

4.1 Injected gas densities (when assuming uniform material deposition), initial electron density, argon fraction, initial plasma temperature, initial plasma current, and toroidal magnetic field strength for six JET discharges. 26

1

Introduction

Plasma, often referred to as the fourth state of matter, is the most common state of matter in the universe, where it seems that 99% of all visible matter is currently in the plasma state (Anderson et al., 2008). For example, it is what stars are made of. In essence, a plasma is an ionized gas consisting of charged particles—ions and electrons. Unlike the solid, liquid, and gaseous states the dynamics of plasmas are highly dependent on electromagnetic forces. This means that plasmas may, in certain circumstances, be modelled with the same equations as liquids and gases, but under the additional constraint of Maxwell's equations.

Plasma physics combines electromagnetism, fluid mechanics, and statistical physics to realistically model and explain observed phenomena. This field of physics has a wide range of applications, from microchips in our computers that rely on plasma-etched semiconductors to the way we use it to study plasmas in space. Moreover, plasma physics plays an important role in the renewable energy sector, where the forefront of research partly concerns fusion energy. The goal of fusion energy research is to create a clean energy source that is able to meet the energy needs of humanity. The two most researched approaches in fusion energy are: Magnetic Confinement Fusion (MCF), that operates practically continuously using low density but high temperature plasmas, and Inertial Confinement Fusion (ICF), where fusion is achieved under extremely high pressures on a very short timescale. In this thesis our focus will be on the prior.

The tokamak device is one of the most widely researched devices for achieving MCF energy, and it is designed to confine the plasma in a torus (doughnut) shape using magnetic fields (Energy.gov, 2023; Greenwald, 2016). The name "tokamak" comes from Russian and is an abbreviation for "toroidal chamber with magnetic coils" (Merriam-Webster, 2024). By using strong magnetic fields to contain and control the high-energy plasma, tokamaks prevent the hottest regions of the plasma from coming into contact with any material surfaces, thus allowing it to reach the extreme temperatures and densities necessary for fusion reactions to occur at a sufficiently high rate. Figure 1.1 shows an illustration of a tokamak, and its magnetic field lines. The toroidal and poloidal magnetic fields are orthogonal components of the total magnetic field. When combined, they give rise to a total magnetic field which is helical. This ensures that the plasma does not drift into the reactor wall, potentially damaging it.

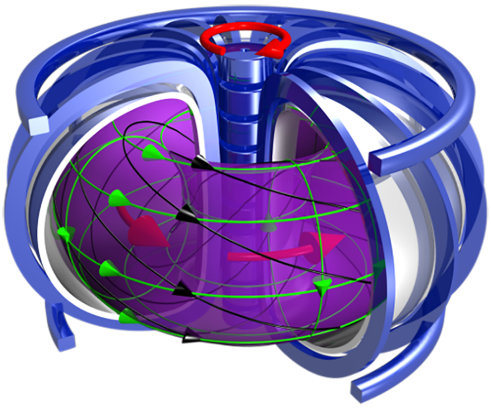

Figure 1.1: Illustration of a tokamak, showing the plasma current (red arrows within the purple plasma) and the magnetic field components: the toroidal field (green arrows parallel to the red arrows), the poloidal field (green arrows orthogonal to the red arrows) and the helical field (black arrows). Image from: Max Planck Institute for Plasma Physics, Germany.

The JET (Joint European Torus) tokamak at Culham centre for Fusion Energy, UK, is a collaborative project among European countries, and was the largest magnetic confinement fusion experiment in the world between 1983 and 2023. It began operation with the hopes of achieving scientific break-even, where the fusion energy gain factor $Q = 1.0$ (i.e. output power per input power) (European Union, 2008). Over the years, a series of improvements were made to JET. In October 2023 it set a new record by producing 69.29 MJ of energy over 6 seconds (EUROfusion, 2024). However, in December 2023 JET finished operations, and decommissioning is expected to last until 2040 (Crepaz, 2023).

Despite this, fusion energy research is more active than ever with many new reactor-scale devices planned for the future and some currently under construction. Two such reactor-scale devices include SPARC (Creely et al., 2020), a compact high-magnetic field device constructed by Commonwealth Fusion Systems in close collaboration with MIT in the USA, and ITER (ITER, 2023), a reactor-scale device under construction in France. Another reactor-scale device is STEP (Spherical Tokamak for Energy Production) (Andrei, 2019), being developed by the UK Atomic Energy Authority. Common for these future tokamaks is that they are expected to produce net energy gain ($Q > 1$). ITER will be the largest among the next generation fusion reactors, and it will manage significantly higher energy compared to present day devices, which therefore also increases the risks and severity associated with so-called plasma-terminating disruptions (Vallhagen, 2023).

Disruptions begin with a sudden loss of plasma confinement, leading to stored thermal energy being dispersed to the surrounding reactor wall (Reux et al., 2015). As a result, the temperature of the tokamak wall material increases, causing the release of impurities which can further cool the plasma. An impurity is any material that is not hydrogen. The cooling results in a reduced electrical conductivity, which means that the plasma current must drop. According to Faraday's law, this induces a strong toroidal electric field, which can accelerate electrons to extremely high energies. Such high-energy electrons, called runaway electrons (REs), pose a major risk to the operation of the tokamak. In order to produce REs, a critical threshold in the induced electric field must be exceeded. In that case, the braking friction force on the electrons from collisions with other plasma particles is no longer enough to overcome the force from the electric field (Chen, 1974). Once formed, REs can further accelerate, and through close collisions with thermal electrons, they can generate additional energetic electrons (secondary generation). This process can result in an exponential increase in the number of REs, called an avalanche (Chen, 1974).

The dynamics of RE beam formation in tokamaks is significantly influenced by the plasma current. In present day tokamaks with plasma currents of a few megaamperes, REs undergo an avalanche gain of a factor of about 5. However, this amplification is expected to be much larger, potentially several orders of magnitude greater, in next-generation tokamaks with substantially higher plasma currents. This is because the avalanche gain is exponentially sensitive to the initial plasma current (Hender et al., 2007; Pusztai et al., 2022). This poses a serious challenge since REs could cause significant damage to plasma-facing components in larger devices. Repairing a reactor wall is both expensive and time-consuming, and can lead to a long shutdown of the reactor. To address this, control measures such as Massive Material Injection (MMI) or magnetic perturbations are necessary (Chen, 1974).

Developing a deeper understanding and more accurate modelling of REs is crucial for advancing safe tokamak operations. Given the urgency of addressing disruption issues in future tokamaks, it is important to develop robust models of REs and disruptions that can inform the design of these reactors. Current tokamak experiments are vital in this endeavour, as they provide a testing ground for validating models and simulating both normal and off-normal operational scenarios on a smaller scale. By comparing model predictions to measurements from existing devices, these experiments can help ensure the success of future reactors.

1.1 Purpose

In this thesis we model the RE existence condition in JET discharges (a tokamak experimental run) using JET discharge #85943 as a baseline case, although the results are not specific to this discharge. To do this, we employ the numerical tool DREAM (*Disruption Runaway Electron Analysis Model*) (Hoppe et al., 2021), which evolves the electron distribution function, temperatures and electric fields self-consistently. The inputs to DREAM are the initial profiles of the plasma currents, particle densities, temperatures, magnetic geometry, transport coefficients, the electrical properties of the wall, and the parameters describing the material injection. We analyze and compare the simulation results with data from an experimental analysis by Reux et al., 2015. The data from the analysis of Reux et al., 2015 for the RE current existence domain is shown in figure 2 in their article and also in figure 4.1 in section 4.1.1. We are interested in how much current is carried by

REs after a disruption and how this depends on the magnetic field strength, initial plasma current and the ratio of injected argon to deuterium.

1.2 Outline

In chapter 2, we present the underlying plasma and tokamak theory necessary to understand disruptions. Chapter 3 gives an overview of DREAM, presenting its physics content and the most important numerical aspects. Chapter 4 begins by presenting the experimental data, followed by a description of our simulation model. Chapter 5 presents the results and discusses our findings. In chapter 6, we summarize our most important findings and provide an outlook with possible future directions and generalizations of the current work.

2

Plasma and tokamak theory

Before we dive into the numerical analysis of plasma disruptions and runaway electron dynamics, we start by going through some of the fundamentals of plasma physics, as well as material relevant for the study of disruptions, runaway electrons and tokamak fusion energy.

2.1 What is plasma physics?

Plasma physics is, simply put, the study of ionized gases, where ionization means that an atom loses one or more of its electrons, forming a positively charged ion. Plasma is often referred to as the fourth state of matter—going one above a regular gas in the hierarchy of states: solid, liquid, gas, and then plasma. Loosely speaking, transitions occur between these states by a change in temperature, where typically solids form at low temperatures and gases at high temperatures. By further increasing the temperature a gas will, due to the high energy of the individual particles, start to ionize and hence form a plasma.

The ionization degree of a gas can be expressed through the Saha equation

$$\left(\frac{n_\mathrm{i}}{n_\mathrm{n}}\right)^2 = 2.4 \cdot 10^{15} \cdot \frac{(T[\mathrm{K}])^{3/2}}{n_\mathrm{n}[\mathrm{m}^{-3}]} \exp\left(-\frac{U_\mathrm{i}}{k_\mathrm{B}T}\right), \tag{2.1}$$

which gives a relation between the degree of ionization of a gas and its temperature T. Here n_i is the number density of ions, n_n is the number density of neutral atoms, T is the temperature in K (note that in plasma physics temperature is usually given in eV, where $1[\mathrm{eV}] \approx k_\mathrm{B}[\mathrm{eV/K}] \cdot 11605$ [K], i.e. 1 eV $\sim$ 11605 K), U_i is the ionization energy for the gas, and k_B is the Boltzmann constant (Bellan, 2008; Anderson et al., 2008). For reference, $U_\mathrm{i} = 13.6$ eV for hydrogen gas.

From the Saha equation we see that the degree of ionization $n_\mathrm{i}/n_\mathrm{n}$ depends strongly on the exponential factor. The degree of ionization varies very sharply for $k_\mathrm{B}T \approx U_\mathrm{i}$; it is very close to zero when $k_\mathrm{B}T \ll U_\mathrm{i}$, and is very high when $k_\mathrm{B}T \gg U_\mathrm{i}$. The temperatures that are required to reach the plasma state lie in the range $T \sim 10^4 - 10^5$ K, because the ionization energy for most gases lies in the range $1-10$ eV (Anderson et al., 2008). However, due to n_n in the denominator, it is also possible for a plasma to form at lower temperatures if the density is kept low.

Plasmas can be observed in many naturally occurring phenomena on Earth, such as lightning discharges and aurorae. Moreover, plasma physics has a wide range of applications, from lasers and modern semiconductor technology to the way we use it to study plasmas in space. A particularly important application of plasma physics is fusion energy research, that aims to replicate the processes that power the Sun.

In fusion, specific atomic nuclei combine to form one or more atomic nuclei, along with subatomic particles such as protons and neutrons. The fusion of deuterium and tritium, known as the D-T reaction, is particularly important in fusion research because it requires the least demanding conditions. This reaction produces a helium-4 nucleus, a neutron, and a significant amount of energy, approximately 17.59 MeV (Shultis and Faw, 2002). This energy is a direct consequence of the mass-energy equivalence principle, coming from Einstein's equation $E = mc^2$, which is consistent with that the observed energy release is due to a reduction in mass.

In the Sun, gravity confines the plasma, which provides the necessary pressure needed to maintain fusion reactions for a long period of time. The fusion reaction rate remains very low until the plasma reaches temperatures around 10^8 K. On Earth, replicating conditions using gravity is not a viable option. Instead, one option is to use magnetic confinement as a means to hold and confine the plasma. The fundamental challenge in fusion energy research is to create plasmas with extremely high temperatures and at the same time sufficiently high densities ($\sim 10^{20}$ m^{-3}) and energy confinement times (~ 1 s) (Bellan, 2008).

2.2 The basics of plasma physics

Although a plasma is an ionized gas, in order for the typical plasma properties to dominate the physics of the gas, certain conditions have to be fulfilled. One way of defining a plasma is the following: "A plasma is a quasi-neutral medium consisting of charged and neutral particles exhibiting collective behaviour" (Anderson et al., 2008). We now discuss what the terms quasi-neutral and collective behaviour mean in the context of plasma physics.

Quasi-neutrality means that plasmas are electrically neutral on a macroscopic scale, despite there being localized charge imbalances at the microscopic scale (Bellan, 2008). When a positively charged ion is introduced into a plasma, it attracts electrons and repels other ions, forming a surrounding cloud of negative charge. This phenomenon is known as Debye screening. The cloud screens the ion's charge, diminishing its electrical influence as observed from a distance. Thus, the overall effect is charge neutrality on sufficiently large spatial scales despite the individual charged particles within the plasma.

The Debye length λ_{D} is a measure of the distance over which electric fields are screened out in a plasma. It represents the scale at which charge carriers (electrons and ions) rearrange themselves to shield out external electric fields. The Debye length is defined as:

$$\lambda_{\mathrm{D}} = \sqrt{\frac{\varepsilon_0 k_{\mathrm{B}} T}{n_{\mathrm{e}} e^2}}, \tag{2.2}$$

where ε_0 is the vacuum permittivity and e is the electron charge.

The term collective behaviour refers to a fundamental distinction between plasma and neutral gases in terms of particle interaction dynamics. Unlike in a neutral gas, where particles interact by pairwise nearly instantaneous collisions characterized by short-range forces, a plasma particle is subject to simultaneous interactions with many other charged particles. This increased amount of interactions arises due to the inherent long-range nature of the electrostatic forces within the plasma (Chen, 1974). Consequently, this collective interaction is fundamental for many of the unique physical properties and phenomena observed in plasma systems. We will discuss some of these properties and phenomena in section 2.4, but first we will review some of the fundamentals of tokamak physics.

2.3 Magnetic confinement in a tokamak

Magnetic confinement in a tokamak is a method used to maintain a high-temperature plasma necessary for nuclear fusion. In a tokamak, a helical magnetic field in a toroidal chamber is used to maintain the plasma, as shown in figure 1.1. When a charged particle, such as an electron or ion with charge e_a (a = e, i), moves within this magnetic field, it experiences the Lorentz force $F = e_a \boldsymbol{v} \times \boldsymbol{B}$ perpendicular to both its velocity and the magnetic field. This force causes the particle to gyrate around the magnetic field lines in a circular motion known as gyro-motion.

A purely toroidal magnetic field is insufficient for stable confinement due to magnetic field inhomogeneities and resulting drifts. Particles would naturally drift away from the centre of the confinement region due to gradients in the magnetic field strength. To eliminate the effect of these drifts and achieve effective confinement, a strong current is driven through the plasma, generating a poloidal magnetic field. The helical field lines resulting from the combined toroidal and poloidal magnetic fields, which are shown in figure 2.1, help maintain the plasma's stability by ensuring that drifts in different sections of the torus counteract each other. The helical magnetic field lines wrap around surfaces of constant poloidal magnetic flux, which is the magnetic flux passing through a surface perpendicular to the poloidal direction in a toroidal plasma. These surfaces are known as flux surfaces, and they are illustrated in figure 2.1. However, during disruptions these flux surfaces can break up due to instabilities, leading to chaotic magnetic fields. This can result in plasma energy being rapidly transported to the reactor wall, potentially causing damage.

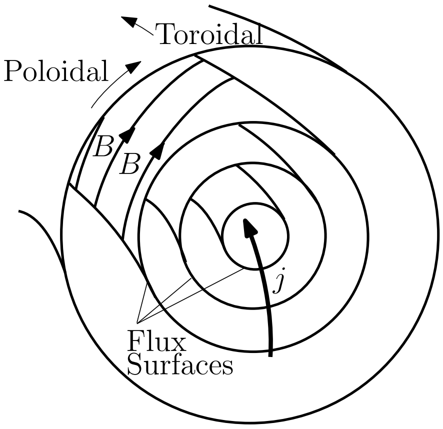

Figure 2.1: Illustration of the tokamak cross-section showing the toroidal and poloidal magnetic fields, which create helical magnetic field lines around the plasma, forming flux surfaces. Source: (Vallhagen, 2023).

The drifts that affect particle motion in a tokamak are:

1. **$\nabla \boldsymbol{B}$-drift (Grad-B-drift)**: Due to the magnetic field strength varying over the major radius of the tokamak, particles experience a drift perpendicular to both the magnetic field and its gradient. This drift is charge-dependent and causes charge separation, leading to an internal electric field.

2. **$\boldsymbol{E} \times \boldsymbol{B}$-drift**: The internal electric field generated by charge separation, in combination with the magnetic field, results in a drift that is independent of the particle's charge, and it can lead to plasma displacement.

3. **Curvature-drift**: As particles follow the curved magnetic field lines of the tokamak, they experience a centrifugal force that causes them to drift perpendicularly to both the magnetic field and the centrifugal force.

2.4 A theoretical description of plasmas

In this section most of the basic plasma physics concepts are introduced as in Anderson et al., 2008. We previously emphasised the collective nature of plasma behaviour. Within a plasma, each particle interacts not only with externally applied fields but also with fields generated by the collective movement of other particles within the same plasma. These interactions can lead to localized charge imbalances, which in turn induce electric fields. Moreover, the motion of charged particles generates electric currents and, consequently, magnetic fields. The dynamics of the particles in a magnetic confinement fusion plasma are well described by classical physics.

In a plasma, the motion of charged particles under the influence of electromagnetic fields is described by the Lorentz force

$$\boldsymbol{F} = e_a(\boldsymbol{E} + \boldsymbol{v} \times \boldsymbol{B}). \tag{2.3}$$

The fundamental (non-relativistic) equation of motion is governed by this force. For a particle with charge e, mass m, moving at velocity $\boldsymbol{v}$ in an electric field $\boldsymbol{E}$ and magnetic field $\boldsymbol{B}$ the equation of motion is

$$m\frac{\mathrm{d}\boldsymbol{v}}{\mathrm{d}t} = e(\boldsymbol{E} + \boldsymbol{v} \times \boldsymbol{B}). \tag{2.4}$$

The dynamics of electromagnetic fields are governed by Maxwell's equations

Gauss's law for electricity: $$\nabla \cdot \boldsymbol{E} = \frac{\rho}{\varepsilon_0}, \tag{2.5}$$

Gauss's law for magnetism: $$\nabla \cdot \boldsymbol{B} = 0, \tag{2.6}$$

Faraday's law of induction: $$\nabla \times \boldsymbol{E} = -\frac{\partial \boldsymbol{B}}{\partial t}, \tag{2.7}$$

Ampère's circuital law (+ Maxwell's correction): $$\nabla \times \boldsymbol{B} = \mu_0 \boldsymbol{j} + \mu_0 \varepsilon_0 \frac{\partial \boldsymbol{E}}{\partial t}, \tag{2.8}$$

where ρ is the charge density, $\boldsymbol{j}$ denotes the current density and μ_0 is the permeability of free space.

In principle, plasma dynamics could be described by solving (2.4) for every particle, considering both external fields and fields generated by the plasma itself. For N particles, there are N nonlinear coupled differential equations of motion to solve simultaneously. However, this would require a self-consistent formulation since the fields and the trajectories of the particles are coupled, which means that internal fields that affect the particles' motion are modified by the particles' collective behaviour (Anderson et al., 2008). Solving (2.4) for every particle is not very practical due to the large amount of particles in a plasma. In tokamak research, it is more common to describe the collective behaviour of particles using statistical physics.

2.4.1 Kinetic theory

Kinetic theory, which comes from statistical mechanics, significantly reduces the analytical complexity compared to solving (2.4) for every particle. This approach utilizes the distribution function $f(\boldsymbol{r}, \boldsymbol{v}, t)$—a statistical representation of the particles in phase space. The main task involves solving the kinetic equations for the various particle species that describe how the distribution function evolves over time.

The distribution function $f(\boldsymbol{r}, \boldsymbol{v}, t)$ specifies the probability density of particles within a small volume element $\mathrm{d}^3r\mathrm{d}^3v$ at position $\boldsymbol{r}$, velocity $\boldsymbol{v}$ and time t in phase space (Anderson et al., 2008). The function f is fundamental in the sense that all macroscopic properties of the plasma can be derived by taking integral moments with respect to velocity of f. For example, the particle number density $n(\boldsymbol{r}, t)$ is obtained by integrating f over all velocities

$$n(\boldsymbol{r}, t) = \int \mathrm{d}^3v\, f(\boldsymbol{r}, \boldsymbol{v}, t). \tag{2.9}$$

Consequently, the total particle number $N(t)$ within the plasma at any given time t is given by

$$N(t) = \int \mathrm{d}^3r\, n(\boldsymbol{r}, t) = \iint \mathrm{d}^3r \mathrm{d}^3v\, f(\boldsymbol{r}, \boldsymbol{v}, t). \tag{2.10}$$

Other important macroscopic quantities include

$$\text{Mean velocity}\, \boldsymbol{u}(\boldsymbol{r}, t) = \frac{1}{n(\boldsymbol{r}, t)} \int \mathrm{d}^3v\, \boldsymbol{v} f(\boldsymbol{r}, \boldsymbol{v}, t), \tag{2.11}$$

$$\text{Pressure tensor}\, \boldsymbol{P}(\boldsymbol{r}, t) = m \int \mathrm{d}^3v\, (\boldsymbol{v} - \boldsymbol{u})(\boldsymbol{v} - \boldsymbol{u}) f(\boldsymbol{r}, \boldsymbol{v}, t), \tag{2.12}$$

$$\text{Energy density}\, W(\boldsymbol{r}, t) = \frac{m}{2n(\boldsymbol{r}, t)} \int \mathrm{d}^3v\, |\boldsymbol{v} - \boldsymbol{u}|^2 f(\boldsymbol{r}, \boldsymbol{v}, t), \tag{2.13}$$

$$\text{Heat flux vector}\, \boldsymbol{Q}(\boldsymbol{r}, t) = \frac{m}{2} \int \mathrm{d}^3v\, |\boldsymbol{v} - \boldsymbol{u}|^2 (\boldsymbol{v} - \boldsymbol{u}) f(\boldsymbol{r}, \boldsymbol{v}, t), \tag{2.14}$$

where (2.12), (2.13), (2.14) only hold in the non-relativistic limit.

An important aspect of plasmas is that when plasma particles are in thermodynamic equilibrium they follow a Maxwell distribution

$$f_{\mathrm{M}}(v) = \left(\frac{1}{\pi v_{\mathrm{th}}^2}\right)^{3/2} \exp\left(-\frac{v^2}{v_{\mathrm{th}}^2}\right). \tag{2.15}$$

Here, we introduced the thermal velocity, which is the average velocity of the plasma particles that follow the Maxwell distribution, for a given particle species $a = \mathrm{e}, \mathrm{i}$ (electron, ion)

$$v_{\mathrm{th},\, a} = \sqrt{\frac{2T_a}{m_a}}, \tag{2.16}$$

where T_a and m_a are the temperature and the mass of the particle respectively.

The time evolution of the distribution function f is described by the kinetic or Boltzmann equation

$$\frac{\partial f}{\partial t} + \boldsymbol{v} \cdot \nabla f + \frac{\boldsymbol{F}}{m} \cdot \nabla_v f = C(f) + S, \tag{2.17}$$

where $\boldsymbol{F}$ is the Lorentz force, the Boltzmann collision operator $C(f)$ describes the effects of particle collisions, and the source term S accounts for variations in particle number resulting from phenomena such as ionization and recombination (Chen, 1974). Recombination means that an electron binds with an ion.

The Boltzmann equation is often simplified by using the Fokker-Planck collision operator, giving the more manageable Fokker-Planck equation. This approximation assumes that collisions in the plasma are dominated by small-angle (grazing) collisions, i.e. collisions only transfer a small amount of momentum. These small-angle scattering events can be represented by a differential operator in velocity space as follows

$$C(f) = \frac{\partial}{\partial v_k} \left[-A_k f + \frac{\partial}{\partial v_l} (D_{kl} f) \right], \tag{2.18}$$

where the advection and diffusion coefficients are given by

$$A_k = \frac{\langle \Delta v_k \rangle}{\Delta t}, \quad D_{kl} = \frac{\langle \Delta v_k \Delta v_l \rangle}{2\Delta t}, \tag{2.19}$$

and k and l are summed indices (Helander and Sigmar, 2005). In this description, the first term in equation (2.18) represents a drag or frictional force acting on the particles, and the second term characterizes diffusion within velocity space. The terms $\langle \Delta v_k \rangle$ and $\langle \Delta v_k \Delta v_l \rangle$ denote the expected change in velocity due to collisions over a short interval Δt, which captures the impact of many small interactions among the plasma particles.

Finally, we mention fluid theory which is a simplified version of kinetic theory—where the particle velocities are averaged over. By taking integral moments with respect to velocity of the Boltzmann equation, one obtains fluid equations. An advantage of this theory is the reduced analytical complexity compared to kinetic theory.

2.4.2 Collisions and conductivity

We have already seen that plasma dynamics differ fundamentally from that of other states of matter. Compared to gases, where collisions are governed by short-range forces, plasma interactions are mainly regulated by long-range Coulomb forces. As a result, high-energy plasma electrons exhibit lower collisionality compared to low-energy plasma electrons—a behaviour opposite to that of neutral particles in regular gases. This distinction is crucial for understanding plasmas, particularly in the extreme environments of reactor-scale tokamaks. To improve our understanding of tokamak plasmas, we will briefly examine particle collisions in plasmas and investigate the resulting physical phenomena.

We start by discussing the collision frequency for electron-electron (e - e) and electron-ion (e - i) Coulomb interactions. The momentum of individual electrons is mainly affected by many small-angle collisions (Helander and Sigmar, 2005). However, when dealing with high-energy electrons one may consider an effective potential to describe the average impact of all particles in the plasma. The collision frequency is given by the expression

$$\nu_{a,b} = \frac{n_b e_a^2 e_b^2 \ln \Lambda}{4\pi \varepsilon_0^2 m_a^2 v_{\mathrm{th},\,a}^3} = \frac{n_b e_a^2 e_b^2 \ln \Lambda}{8\pi \varepsilon_0^2 \sqrt{2 m_a} T_a^{3/2}} \tag{2.20}$$

where n_b represents the density of particle species b and e_a and e_b are the electric charges of particle species a and b respectively (Helander and Sigmar, 2005). Finally, $\ln \Lambda$ is the Coulomb logarithm which quantifies the maximum impact parameter of Coulomb collisions (Chen, 1974).

Equation (2.20) contains the $T^{-3/2}$ temperature scaling, which is crucial in the context of tokamak disruptions. The conductivity of the plasma, which was first formulated by Lyman Spitzer (Cohen et al., 1950; Spitzer and Härm, 1953), is given by

$$\sigma \sim \frac{n_\mathrm{e} e^2}{m_\mathrm{e} \nu_\mathrm{e,\,i}} \sim T^{3/2} \tag{2.21}$$

(Helander and Sigmar, 2005), and this expression implies that as the plasma temperature drops its conductivity decreases. According to Ohm's law

$$\boldsymbol{j} = \sigma \boldsymbol{E}, \tag{2.22}$$

a lower conductivity must give rise to a proportionally higher induced electric field to maintain the same current (Chen, 1974). This compensation effect is important because, in a plasma environment like that of a tokamak, the current cannot change instantaneously. If the temperature of the plasma suddenly drops rapidly, which it commonly does during a disruption, an electric field will be induced. This force will accelerate plasma electrons to relativistic energies, in a process that leads to the formation of a beam of REs (Vallhagen, 2023).

2.4.3 Electron runaway

Super-thermal electrons, those electrons with velocity $v \gg v_\mathrm{th}$, feel a braking drag force proportional to

$$F_\mathrm{drag} \sim m_\mathrm{e} v \nu_{\mathrm{e},\,b} \propto v^{-2}, \tag{2.23}$$

due to Coulomb interactions—which normally decelerate them (Helander and Sigmar, 2005). However, when these electrons exceed a critical velocity, where an externally applied electric field's accelerating force is stronger than the drag force, they can be accelerated to relativistic velocities (Anderson et al., 2008). This scenario leads to an unlimited acceleration of electrons to very high energies, where non-collisional mechanisms determine the electron dynamics.

To better understand the above scenario, we may study the one-dimensional dynamics of an electron under the forces of an externally applied electric field $\boldsymbol{E} = -E\hat{\boldsymbol{x}}$ and collisional drag F_drag (2.23). Newton's second law gives

$$m_\mathrm{e} \frac{\mathrm{d}v}{\mathrm{d}t} = eE - m_\mathrm{e} v \nu_\mathrm{e,\,i}, \tag{2.24}$$

which can be rewritten by using (2.20) and (2.23) to give

$$m_\mathrm{e} \frac{\mathrm{d}v}{\mathrm{d}t} = eE \left(1 - \frac{v_\mathrm{c}^2}{v^2}\right), \tag{2.25}$$

where we defined v_c as the critical velocity

$$v_\mathrm{c}^2 = \frac{\pi n e^3 \ln \Lambda}{(4\pi\epsilon_0)^2 m_\mathrm{e} E}. \tag{2.26}$$

The critical velocity is the velocity where the electric force equals the collisional drag force. When the electron's velocity v is less than v_c the velocity will tend to decrease due to the larger friction force compared to the accelerating electric force. On the other hand, if v is greater than the critical velocity the electron experiences a net acceleration ($\mathrm{d}v/\mathrm{d}t > 0$), reducing the effective drag as the velocity increases. This case allows for the continuous acceleration of the electron to relativistic energies (Anderson et al., 2008). When the friction force becomes weaker with the increasing speed of the electron, the phenomenon is called electron runaway, and is a major concern for future large-scale tokamaks. Electrons with velocities greater than the critical velocity are known as runaway electrons, and they may lose magnetic confinement and damage the reactor's wall, leading to high repair costs and long operational downtime (Chen, 1974).

To further our understanding of the implications of electron runaway, we may compare the critical velocity v_{c} with the thermal velocity of electrons $v_{\mathrm{th,\,e}}$. If the thermal velocity is significantly less than the critical velocity ($v_{\mathrm{th,\,e}} \ll v_{\mathrm{c}}$), then only a small amount of electrons at the upper end of the Maxwell distribution are likely to become runaway. However, when the critical velocity approaches the thermal velocity ($v_{\mathrm{c}} \approx v_{\mathrm{th}}$) a substantial portion of the electron population would be subjected to acceleration.

The electric field strength at which the critical velocity equals the thermal velocity is defined as $0.215E_{\mathrm{D}}$, where E_{D} is the Dreicer field

$$E_{\mathrm{D}} = \frac{\pi n e^3 \ln\Lambda}{(4\pi\epsilon_0)^2 k_{\mathrm{B}} T}. \tag{2.27}$$

The fraction E/E_{D} becomes significant (but still much smaller than unity) during plasma disruptions.

If one includes relativistic effects then the drag force does not fall all the way down to zero with increasing electron energy—since there is some saturation that occurs when electrons approach the speed of light (Helander and Sigmar, 2005). This implies that there is a minimum electric field for the creation of REs, which produces the same acceleration as the collisional drag at the speed of light. The electric field is called the critical electric field E_{c} and is given by

$$E_{\mathrm{c}} = \frac{n e^3 \ln\Lambda}{4\pi\epsilon_0^2 m_{\mathrm{e}} c^2}, \tag{2.28}$$

where c is the speed of light (Connor and Hastie, 1975). Thus, in order to produce REs an electric field must exceed the critical field.

2.5 Runaway generation mechanisms

Runaway electron generation in tokamaks arises through various mechanisms. These mechanisms can be broadly classified into primary (seed) and secondary (avalanche) mechanisms. Primary generation occurs independently of existing REs, while secondary generation relies on an initial population of REs to increase in number.

The following sections detail the most significant runaway generation mechanisms in tokamaks.

2.5.1 Primary generation mechanisms

Dreicer mechanism: The Dreicer mechanism describes the process by which an electric field accelerates electrons to runaway velocities, overcoming the collisional friction in the plasma (Dreicer, 1959). As the electric field strength increases, a fraction of electrons in the high-energy tail of the Maxwellian distribution can accelerate past the critical velocity v_c and continue to gain energy, thereby becoming REs. This process is self-sustaining because the remaining electron population continually re-equilibrates the Maxwellian due to particle collisions, thus maintaining the high-energy tail and consequently RE generation.

Hot-tail mechanism: The hot-tail mechanism occurs during rapid and steep plasma temperature drops. Initially, the high-energy tail of the Maxwellian, being at a higher temperature, cools more slowly than the bulk population. This results in a temporary non-Maxwellian distribution with an excess of super-thermal electrons. If an external electric field increases in strength, these super-thermal electrons can surpass the critical velocity and become REs before thermalizing with the cooler bulk electrons (Smith and Verwichte, 2008; Smith et al., 2005). The efficiency of hot-tail generation depends on the rate of temperature decrease, with faster drops generally leading to higher RE production (Svenningsson et al., 2021).

Tritium decay and Compton scattering: In deuterium-tritium (D-T) plasmas, tritium decay and Compton scattering can also generate REs. Tritium decay produces high-energy electrons that, if exceeding the critical velocity threshold, become runaway electrons (Fülöp et al., 2020). Additionally, gamma photons resulting from neutron interactions with the tokamak wall can scatter electrons via the Compton effect, transferring sufficient energy to make the electrons runaways (Martín-Solís et al., 2017).

2.5.2 Secondary generation mechanism

Avalanche: The avalanche mechanism can drastically increase the population of REs. During a Coulomb collision, a runaway electron can transfer significant momentum to a thermal electron, accelerating it above the critical velocity. If the electric field is sufficiently strong, this process becomes self-sustaining with each new runaway electron potentially generating more REs, which leads to an exponential increase in the RE population. Moreover, avalanche gain is exponentially sensitive to the strength of the initial plasma current in a tokamak. The avalanche effect is particularly dominant during the current quench (CQ) phase of a disruption (to be discussed in the next section) in large tokamaks, and poses a significant challenge in controlling runaway currents (Embréus et al., 2018; Rosenbluth and Putvinski, 1997). Minimizing the initial number of REs during a disruption is very important to prevent the avalanche from producing excessive runaway currents.

In summary, mitigating these runaway generation mechanisms is vital for the safe operation of tokamaks, particularly as we move towards larger devices such as ITER, which will operate with much larger plasma currents compared to current tokamaks. Hence for future large-scale reactors, controlling REs becomes even more important for preventing damage of the plasma facing components.

2.6 Tokamak disruptions

Tokamak disruptions are abrupt and often violent events that lead to the loss of plasma confinement. These disruptions result from too high plasma density, large plasma currents or the accumulation of heavy impurities, leading to a sudden release of energy, loss of plasma confinement and potential damage to the tokamak's internal components (Koslowski, 2012; Hender et al., 2007). An impurity is any material that is not hydrogen. Figure 2.2 illustrates a typical disruption evolution along with the behaviour of the electron temperature T_e, induced electric field $E_\|$, plasma current I_p, Ohmic current I_Ω, and runaway current I_RE. The Ohmic current in a tokamak is the electric current generated by the resistive heating of the plasma due to the applied electric field, analogous to the current produced in a conventional conductor due to Ohm's law.

2.6.1 The three phases of a disruption

The first phase of a disruption is the thermal quench (TQ). During this phase, the plasma experiences a rapid and drastic drop in temperature, typically within a time span of 0.1-1 ms. The sudden decrease in temperature raises the plasma resistivity as particle collisions become more frequent (Hoppe, 2021). The rapid cooling is primarily caused by increased radiation from impurities and heat transport due to magnetic perturbations. The latter refers to disturbances or fluctuations in the magnetic field that can affect plasma stability and confinement.

The CQ (current quench) in a tokamak disruption refers to the phase where the plasma current rapidly decreases due to a significant rise in plasma resistivity. The CQ typically takes place after the TQ phase and happens over a time span of around 10 ms in a JET-sized device. During this phase, the decay of the plasma current results in the formation of induced eddy and halo currents, which in combination with the tokamak's magnetic fields, causing electromagnetic forces that can impose mechanical stresses on the tokamak's components (Shiraki et al., 2016). Moreover, the rapid current decay during the CQ is also important since it impacts the formation of runaway electrons. The high resistivity in the post-TQ plasma environment accelerates the decay of the initial current, and, due to Faraday's law, a current drop must result in an induced electric field. This electric field may lead to the generation of REs, which can cause localized melting of the tokamak wall or other structural damage to the tokamak device (Breizman et al., 2019; Helander et al., 2002; Shiraki et al., 2016).

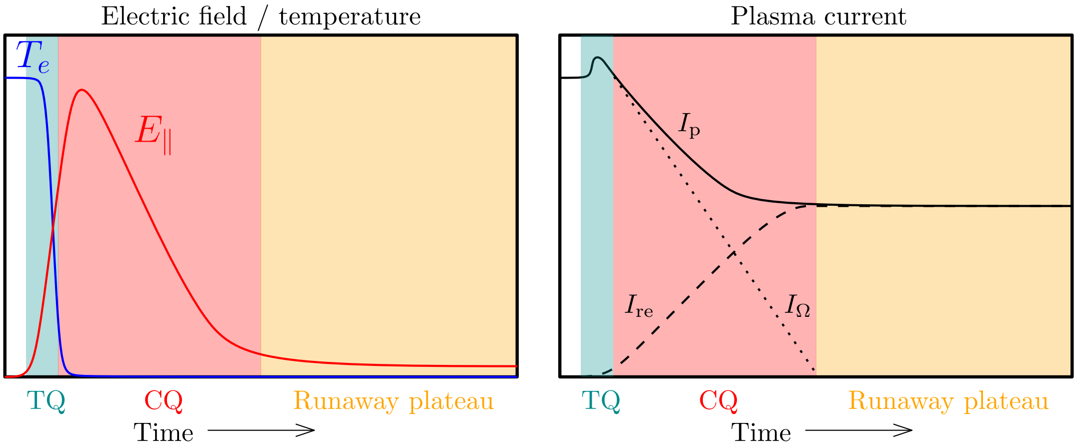

Figure 2.2: Illustration of the typical behaviour of the electron temperature T_e, induced electric field $E_\parallel$, plasma current I_p, Ohmic current I_Ω, and runaway current I_RE during a disruption. Source: (Hoppe, 2021).

The runaway plateau is the final stage of a disruption. During this phase, the RE current can dominate the plasma current if a sufficiently strong induced electric field was sustained during the CQ. This situation is particularly dangerous because REs carry large amounts of energy and momentum.

2.6.2 Miscellaneous

To quantitatively analyze the temperature evolution of the TQ an exponential temperature decay model is often used, given by

$$T(t,r) = T_\mathrm{f}(r) + [T_0(r) - T_\mathrm{f}(r)] \exp\left(-\frac{t}{\tau_\mathrm{TQ}}\right). \tag{2.29}$$

Here, $T_0(r)$ represents the initial temperature profile of the tokamak plasma, which is typically deduced from experimental data. The parameter τ_TQ denotes the decay time scale, giving an estimate of the rate at which the temperature falls during the TQ. The term $T_\mathrm{f}(r)$ refers to the final temperature, which corresponds to the temperature at the onset of the CQ phase. Commonly, T_f is treated as a free parameter and may be set to a constant. However, this model is not explicitly employed in this work. Instead, it is used indirectly to provide a reference point for the thermal quench duration in our disruption model, which will be discussed in more detail in section 4.2.

The duration of the CQ phase t_CQ is defined in this work as

$$t_\mathrm{CQ} = \frac{t_{I_{\Omega,\mathrm{final}}} - t_{I_\Omega = 0.8 I_{\mathrm{p,\,max}}}}{0.8 - I_{\Omega,\mathrm{final}}/I_\mathrm{p,init}} \tag{2.30}$$

where I_p represents the total plasma current and I_Ω denotes the Ohmic current component. A too short CQ time can generate large electromagnetic forces from the eddy or halo currents. Conversely, a prolonged CQ duration increases the risk of plasma drift, leading to potential impacts against the containment wall.

2.7 Disruption mitigation

Managing disruptions in tokamaks involves several strategies to predict, prevent, and mitigate their effects (Lehnen et al., 2015). In this section we discuss a common disruption mitigation technique employed in tokamaks.

2.7.1 Massive material injection (MMI)

Massive material injection, which has been successfully implemented in JET and is planned for future use in ITER involves the deliberate introduction of large quantities of material into the plasma to trigger a controlled cooling disruption. Examples of MMI are Massive Gas Injection (MGI) and Shattered Pellet Injection (SPI), which are employed to rapidly cool the plasma and reduce the current before a disruption can fully develop (Hollmann et al., 2014). Moreover, these methods aim to increase the plasma density, thereby raising collisionality and reducing the likelihood of runaway electron formation. However, it is important to note that injecting impurities into the plasma may also have the opposite effect, namely it can generate additional REs. Therefore, it is crucial to identify the optimal injection conditions that minimize the production of runaway electrons while still maintaining an adequate fusion reaction rate.

MGI introduces large amounts of neutral gases, particularly noble gases like neon or argon, to increase electron density. This gives rise to an increase in collisionality resulting in a greater braking force on the electrons, thereby reducing their energy and decreasing the risk of reactor damage. Furthermore, the introduction of heavier noble gases increases heat loss through radiation (Hu et al., 2021). Note that increased heat loss implies quicker and more significant plasma cooling, which inherently results in a stronger induced electric field, and consequently a higher production of REs. Finally, one may also inject deuterium, which becomes fully ionized at relatively low temperatures, to dilute the plasma. This helps with plasma stabilization by mitigating the more severe radiation losses that heavier atoms might cause (Nardon et al., 2020).

2.7.2 Assimilation of the injected material

Assimilation in tokamak experiments with MGI refers to the process by which injected material are incorporated into the plasma. This process involves several stages, starting with the gas crossing the plasma boundary and distributing uniformly throughout the plasma volume. Upon entering the plasma, the injected gas begins to ionize, allowing it to interact electromagnetically with the existing plasma particles. Successful assimilation is characterized by the thermal and chemical equilibrium of the injected gas with the plasma. This means the gas reaches a uniform temperature distribution and mixes homogeneously with the plasma. The effectiveness of this process directly impacts the efficiency of plasma cooling. For example, impurities that have assimilated well can enhance radiation cooling, which could help in reducing the thermal load on the plasma-facing components and to stabilize the plasma during disruptions (Effenberg, 2022; Zeng et al., 2023).

3

Simulation framework: DREAM

This chapter provides an overview of DREAM (*Disruption Runaway Electron Analysis Model*) (Hoppe et al., 2021). Developed by the Plasma Theory Group at Chalmers University of Technology, DREAM is a simulation framework that models the dynamics of REs during tokamak disruptions. It solves a system of nonlinear equations that govern the time evolution of plasma parameters, including temperature, electron density, current density, and electric fields. Moreover, DREAM supports various operational modes, from a fluid mode to a fully kinetic mode.

More specifically, this chapter aims to provide an overview of the DREAM methods used in our study, primarily based on the theory outlined in the original paper by Hoppe et al., 2021 and the DREAM documentation by Hoppe, 2024. For a comprehensive understanding of DREAM, it is recommended to read both the original paper and the documentation.

3.1 Electron populations and plasma models

DREAM solves the electron distribution function through the Fokker-Planck equation. For efficient computation, DREAM considers three groups of electrons: cold electrons, hot electrons, and REs, each characterized by their respective densities $\langle n_{\mathrm{cold}} \rangle$, $\langle n_{\mathrm{hot}} \rangle$, and $\langle n_{\mathrm{RE}} \rangle$. These groups are ordered by momentum, with cold electrons having the lowest momentum and REs the highest momentum. These electron populations are shown in figure 3.1.

DREAM employs various plasma models that each model the electron populations differently. This work uses the *isotropic mode*, which simplifies computation by analytically averaging over the pitch angle, which refers to the angle between a charged particle's velocity vector and the magnetic field line along which it is travelling, based on an asymptotic expansion where pitch-angle scattering predominates (Hoppe et al., 2021). This assumption considerably reduces the model's complexity and computational cost by decreasing the dimensionality of the distribution function. Although less computationally demanding, the isotropic mode accounts for the essential dynamics that are fully described by more computationally demanding modes, giving a good trade-off between model accuracy and computational cost.

In the isotropic mode, only hot electrons are treated kinetically. In general, kinetic modelling means that the full phase space, including momentum and pitch

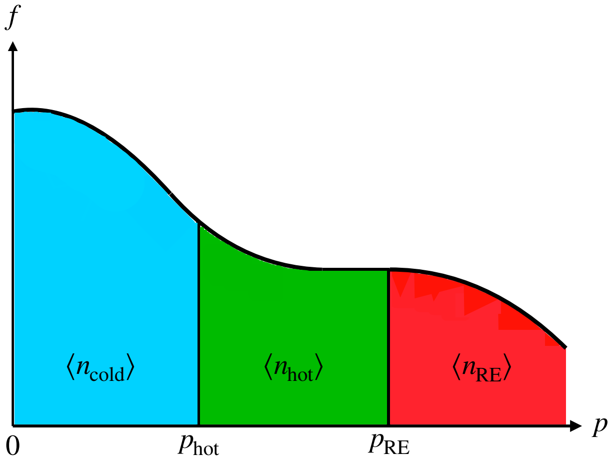
f
$\langle n_{\text{cold}} \rangle$
$\langle n_{\text{hot}} \rangle$
$\langle n_{\text{RE}} \rangle$
p
0
p_{hot}
p_{RE}

Figure 3.1: Electron populations as modelled in DREAM.

angle, is considered in the modelling. However, in the isotropic mode the pitch angle is averaged over. Meanwhile, cold electrons and REs are modelled as fluids. This means that the plasma evolution is not governed by the Fokker-Planck equation, but rather by other self-consistent equations, such as energy conservation and charge neutrality. Since cold electrons are fluid quantities, this implies that the momentum boundary $p_{\text{hot}} = 0$ in the figure 3.1. To model how electrons are transferred from the hot to the cold population, there is a particle sink at $p = 0$ in this mode, which converts hot electrons to cold electrons. Almost all electrons are initialized as hot electrons in an isotropic simulation, and more cannot be created while the simulation is underway. A further motivation for using the isotropic mode is that most of the interesting physics occurs in the hot momentum region. For instance, this is typically where the critical momentum lies under our conditions. Therefore, it is important to model this region kinetically to achieve a realistic disruption model.

As mentioned, cold electrons are characterized by having lower kinetic energy than hot electrons, and they can be assumed to follow a Maxwell distribution, which is characterized by their density $\langle n_{\text{cold}} \rangle$, temperature T_{cold} and the Ohmic current density j_Ω. The density of cold electrons is calculated to preserve net neutrality according to

$$\langle n_{\text{cold}} \rangle = \langle n_{\text{free}} \rangle - \langle n_{\text{hot}} \rangle - \langle n_{\text{RE}} \rangle. \tag{3.1}$$

Here, $\langle n_{\text{free}} \rangle$ represents the total density of free electrons in the plasma, obtained from quasi-neutrality $\langle n_{\text{free}} \rangle = \sum_i Z_{0,i} n_i$, where $Z_{0,i}$ is the charge number, summing over all ion charge states i. The electron temperature on flux surfaces T_{cold} is modelled through the evolution of the thermal energy density of the cold electron population

$$W_{\text{cold}} = \frac{3}{2} \langle n_{\text{cold}} \rangle T_{\text{cold}}. \tag{3.2}$$

Hot electrons, with momentum $p_{\text{hot}} < p < p_{\text{RE}}$, are kinetically modelled using the distribution function f_{hot}. Parameters such as the density of hot electrons n_{hot}

and their current density j_{hot} are obtained as different moments of this function.

REs, which have momentum $p > p_{\text{RE}}$, are assumed to move along magnetic field lines at the speed of light. Moreover, they are represented by the RE density n_{RE} and the current density j_{RE}. For simulations relevant for this work, the time evolution of n_{RE} is governed by

$$\frac{\mathrm{d}n_{\text{RE}}}{\mathrm{d}t} = F_{\text{hot}} + \Gamma_{\text{Ava}} n_{\text{RE}} + \frac{1}{V'}\frac{\partial}{\partial r}\left[V'\left(A n_{\text{RE}} + D\frac{\partial n_{\text{RE}}}{\partial r}\right)\right]. \tag{3.3}$$

The term F_{hot} is the flux of runaways through the upper boundary of the hot momentum grid, so that electrons flow into the runaway region. It combines contributions from the Dreicer and the hot-tail generation mechanisms. The avalanche growth rate is denoted by Γ_{Ava}, radial transport effects, both advective and diffusive, are accounted for with A and D, respectively, and V' denotes the spatial Jacobian at a given radius r.

3.2 Ions

Ion species in DREAM, each identified by an atomic number Z_i, are modelled by their densities $n_i^{(j)}$ for each charge state j. The evolution of the ion states is governed by the ion rate equation

$$\begin{aligned}\frac{\partial n_i^{(j)}}{\partial t} &= \left(I_i^{(j-1)}\langle n_{\text{cold}}\rangle + \langle \sigma_{\text{ion},\,i}^{(j-1)} v\rangle\right) n_i^{(j-1)} \\ &\quad - \left(I_i^{(j)}\langle n_{\text{cold}}\rangle + \langle \sigma_{\text{ion},\,i}^{(j)} v\rangle\right) n_i^{(j)} \\ &\quad + R_i^{(j+1)}\langle n_{\text{cold}}\rangle n_i^{(j+1)} - R_i^{(j)}\langle n_{\text{cold}}\rangle n_i^{(j)},\end{aligned} \tag{3.4}$$

where $I_i^{(j)}$ denotes the ionization rate coefficients and $R_i^{(j)}$ denotes recombination rate coefficients. These rates represent transitions between the different charge states. The rate coefficients come from the OpenADAS database (OpenADAS, 2024). When we involve hydrogen isotopes, such as deuterium, where low-temperature opacity to Lyman radiation is significant, the coefficients come from the AMJUEL database (Reiter, 2000). Lyman radiation refers to the series of spectral lines in the ultraviolet region that are emitted by hydrogen atoms when an electron transitions from a higher energy level ($n \geq 2$) down to the lowest energy level ($n = 1$).

3.3 Poloidal magnetic flux

The evolution of the poloidal magnetic flux ψ is governed by the equation

$$\frac{\partial \psi}{\partial t} = -V_{\text{loop}}. \tag{3.5}$$

The loop voltage V_{loop} is defined as

$$V_{\text{loop}} = 2\pi\frac{\langle \boldsymbol{E}\cdot\boldsymbol{B}\rangle}{\langle \boldsymbol{B}\cdot\nabla\phi\rangle}, \tag{3.6}$$

where ϕ is the poloidal angle. The total current density is given by $j_{\mathrm{tot}} = j_{\Omega} + j_{\mathrm{hot}} + j_{\mathrm{RE}}$, where the time evolution is governed by Ampère's law

$$2\pi\mu_0 \langle \boldsymbol{B} \cdot \nabla\phi \rangle \frac{j_{\mathrm{tot}}}{B} = \frac{1}{V'} \frac{\partial}{\partial r} \left[V' \left\langle \frac{|\nabla r|^2}{R^2} \right\rangle \frac{\partial \psi}{\partial r} \right]. \tag{3.7}$$

Boundary conditions for ψ are set at $\psi_{\mathrm{edge}} = \psi(r = a)$ and $\psi_{\mathrm{wall}} = \psi(r = b)$, where a is the minor radius and b is the wall radius. We assume that the plasma is surrounded by a perfectly conducting wall, which imposes the condition $V_{\mathrm{loop}} = 0$ at $r = b$.

3.4 Magnetic geometry, time stepper and numerical solver

DREAM can employ numerically defined magnetic fields, which allow for the simulation of realistic tokamak geometries—accounting for variations in the magnetic field across different flux surfaces.

Time evolution of the array of unknowns in DREAM is handled through either an adaptive time stepper or a fixed time stepper, where the former is based on an estimate of the ionization time scale (Hoppe et al., 2021).

The system of equations for the next time step is expressed as $\boldsymbol{f}(\boldsymbol{x}(t), t) = 0$, where $\boldsymbol{x}(t)$ is the solution vector. DREAM solves this using Newton's method

$$\boldsymbol{x}_{i+1}^{j+1} = \boldsymbol{x}_{i}^{j+1} - J^{-1}(\boldsymbol{x}_{i}^{j+1}) \boldsymbol{f}(\boldsymbol{x}_{i}^{j+1}) \tag{3.8}$$

where J^{-1} is the inverse Jacobian matrix of the function $\boldsymbol{f}$. Upper indices represent time step and lower indices represent the current approximation. The iteration continues until convergence is reached or until a specified number of iterations have passed. Once converged, the solver checks each obtained solution in the array of unknowns and demands that

$$\left\| \boldsymbol{y}_{i+1}^{(n)} - \boldsymbol{y}_{i}^{(n)} \right\| \leq \epsilon_{\mathrm{abs}}^{(n)} + \left\| \boldsymbol{y}_{i+1}^{(n)} \right\| \epsilon_{\mathrm{rel}}^{(n)}. \tag{3.9}$$

Here $\boldsymbol{y}_{i+1}^{(n)}$ is a subset of the elements in $\boldsymbol{x}_{i+1}$, corresponding to the discretized quantity denoted with index n (Hoppe, 2024). The tolerances for the quantity is the absolute tolerance $\epsilon_{\mathrm{abs}}^{(n)}$ and relative tolerance $\epsilon_{\mathrm{rel}}^{(n)}$, which, along with the maximum number of iterations, may be specified by the user.

3.5 Radial heat transport

In DREAM, radial transport of heat is modelled using an advection-diffusion heat transport approach. For the purposes of this work, the Rechester-Rosenbluth diffusion model is employed to describe this transport mechanism. Developed by Rechester and Rosenbluth, 1978, this diffusion model addresses the radial transport of heat due to turbulent perturbations in the magnetic field. Rechester and Rosenbluth derived a diffusion operator that quantifies how these perturbations affect the motion of particles and energy radially across the plasma. The diffusion coefficient D_{RR} takes the form

$$D_{\mathrm{RR}} = \pi R_0 |v_{\mathrm{th,e}}| \left(\frac{\delta B}{B}\right)^2, \tag{3.10}$$

where R_0 is the major radius of the tokamak. In a similar expression for the RE particle diffusivity, the thermal velocity $v_{\mathrm{th\,e}}$ is replaced with the speed of light c. The factor $\delta B/B$ quantifies the normalized amplitude of magnetic perturbations, which parametrizes the effect of magnetic field fluctuations on transport.

3.6 Synchrotron losses

Synchrotron loss refers to the energy loss experienced by charged particles, such as electrons, when they are accelerated to near-light speeds and move in a circular motion. As these particles gyrate along magnetic field lines, they emit electromagnetic radiation, known as synchrotron radiation. This emission of radiation results in a loss of energy for the particles, thereby damping their motion.

DREAM implements synchrotron loss using the model developed by Hirvijoki et al., 2015 and Decker et al., 2016, which employs the radiation timescale

$$\tau_{\mathrm{rad}}^{-1} = \frac{e^4 B^2}{6\pi\varepsilon_0 m_{\mathrm{e}}^3 c^3}, \tag{3.11}$$

where B is the magnetic field strength. Note that the radiation timescale includes a factor for the gyration frequency of the electrons

$$\omega = \frac{eB}{m_{\mathrm{e}}}. \tag{3.12}$$

This quantity will be important later on, when we discuss the effects of the magnetic field strength on the dynamics of REs.

4

Method

This section presents the experimental data utilized in our study and the disruption modelling with DREAM. Section 4.1 discusses the experimental data obtained for six JET discharges. In section 4.2, we discuss the specific initial conditions, parameters, and configurations used in DREAM to simulate JET disruptions.

4.1 Experimental data

This study uses data for six JET discharges (an experimental run of the tokamak), which come from experiments conducted by Reux et al., 2015. These discharges exhibit different plasma and tokamak parameters, such as initial temperature, electron density, plasma current, magnetic field strength and geometry as well as injected argon to deuterium ratio. All discharges were terminated through MGI. Table 4.1 provides an overview of the parameters associated with these discharges. Note that we have radial profile information on the electron density, the electron temperature and the current density prior to the disruption, where the values listed in the table are taken at the magnetic axis. The temperatures and electron densities are measured using Light Detection And Ranging (LIDAR). The mentioned plasma parameter radial profiles are used as initial conditions for the simulations, and the subsequent disruption evolution is self-consistently simulated by DREAM. Furthermore, the minor and major radii of JET discharge #85943 is $a = 0.895$ m and $R_0 = 2.93$ m, respectively, and note that these geometric values are essentially the same for all discharges.

To initiate disruptions within the JET tokamak, argon gas and deuterium gas were injected into the vacuum vessel, with their quantities G_i specified in Pa m^3. Initially in our simulations, these gases are considered to be at room temperature $T_{\text{init}} = 300$ K. Using the ideal gas law $N_i = G_i/(k_\text{B}T_{\text{init}})$, we can calculate the total number of argon atoms N_{Ar} and deuterium atoms N_D, respectively. For the purpose of simulation, these atomic totals are then used to compute the ion densities by dividing by JET's plasma volume $V_\text{p} = 76.55$ m^3 (this value can also be regarded to be the same for all the discharges), resulting in $n_i = N_i/V_\text{p}$.

Each density n_i is subsequently multiplied by an assimilation fraction f_i, representing the fraction of the gas that gets deposited inside the plasma, giving $n_{i,\,\text{injected}} = f_i n_i$. To find realistic values for f_{Ar} and f_D that give numerically stable solutions, we treat these parameters as free—since they are not known from experiments. All

Table 4.1: Injected gas densities (when assuming uniform material deposition), initial electron density, argon fraction, initial plasma temperature, initial plasma current, and toroidal magnetic field strength for six JET discharges.

Parameter	**#85021**	**#85445**	**#85450**	**#85451**	**#85453**	**#85943**
n_{Ar} $(10^{21}\mathrm{m}^{-3})$	1.62	0.30	1.04	1.64	2.44	2.46
n_{D} $(10^{21}\mathrm{m}^{-3})$	1.08	2.67	1.56	1.09	0	0
$n_{\mathrm{e,0}}$ $(10^{19}\mathrm{m}^{-3})$	1.68	2.21	1.75	1.69	1.50	2.05
$\alpha_{\mathrm{Ar/D}}$	0.6	0.1	0.4	0.6	1.0	1.0
T_0 (eV)	1928	2868	1192	1410	1138	2541
$I_{\mathrm{p,0}}$ (MA)	1.95	1.95	1.69	1.69	1.19	1.95
B_{T} (T)	2.5	3	1.5	1.5	1	3

free parameters in this work are part of a series of parameter scans aimed at finding values for the free parameters that reproduce experimentally observed runaway currents. This is discussed further in chapter 5. Apart from the parameter scans, we are guided by insights from previous studies such as Björk et al., 2021, which suggests an assimilation fraction of 20% for argon—for similar types of JET discharges as the ones we study. To maintain a simple model, we assume an equal assimilation fraction for both injected gases $f_i = f_{\mathrm{Ar}} = f_{\mathrm{D}}$.

4.1.1 Runaway electron existence domain map

We now present the all-important figure 4.1 (reproduced from Reux et al., 2015), which serves as the primary motivation for this thesis. The purpose of this thesis can be seen as an attempt to reproduce this figure through simulation. The figure summarizes the runaway electron existence domain for MGI discharges (some of which are presented in the previous section) of argon and deuterium mixtures, covering various gas pressures, different toroidal field strengths, plasma pre-disruption densities, and shapes for JET-ILW (ITER-like Wall) and JET-C (Carbon wall). A runaway domain boundary is depicted for JET-ILW (green strip) and JET-C (red strip), respectively. Below these boundaries, no significant RE current was observed. In this work, we aim to reproduce the green domain boundary using DREAM, with the goal of enhancing code validation to ensure that our models accurately describe and predict conditions in both existing and future tokamaks. For a full description of the figure, we refer the reader to the original paper by Reux et al., 2015.

4.1.2 Plasma current evolution data

The empirically measured plasma current evolution data for each of the six discharges used is shown in figure 4.2. Note that the data was smoothed to reduce noise. Several points regarding this figure are worth noting.

First, the zero point of the time scale is arbitrary. The onset of the TQ for each discharge is assumed to start at the point where the plasma current starts to decrease slightly, right before each discharge's respective I_{p}-spike. This assumption is based

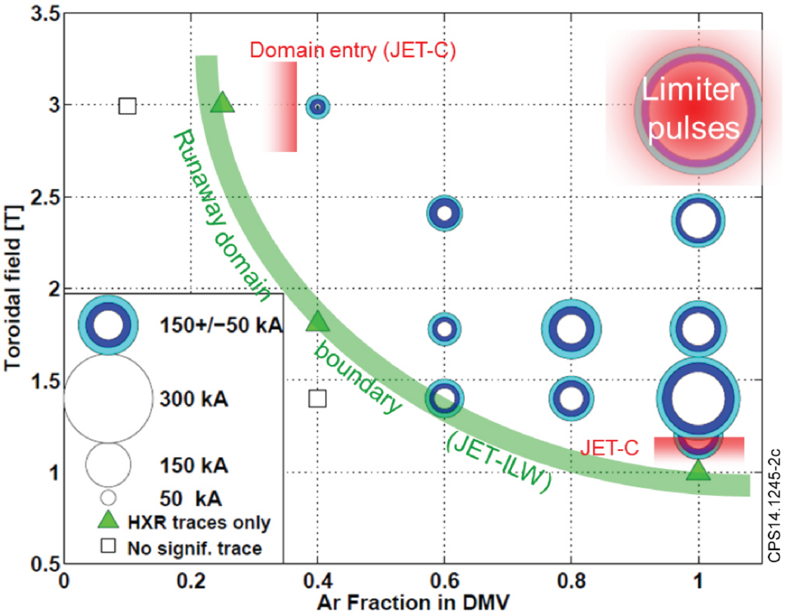

Figure 4.1: Runaway electron existence domain map as a function of toroidal field and argon fraction in the disruption mitigation valve. As an example, an Ar fraction = 0.6 means that 60% of the injected material is argon and 40% is deuterium. Each data point corresponds to a unique discharge, but note that in our work we only used data for six of the displayed discharges. The domain entry points and boundaries are provided for JET-C and JET-ILW. The size of the circles represents the maximum runaway current achieved during a disruption. Source: (Reux et al., 2015).

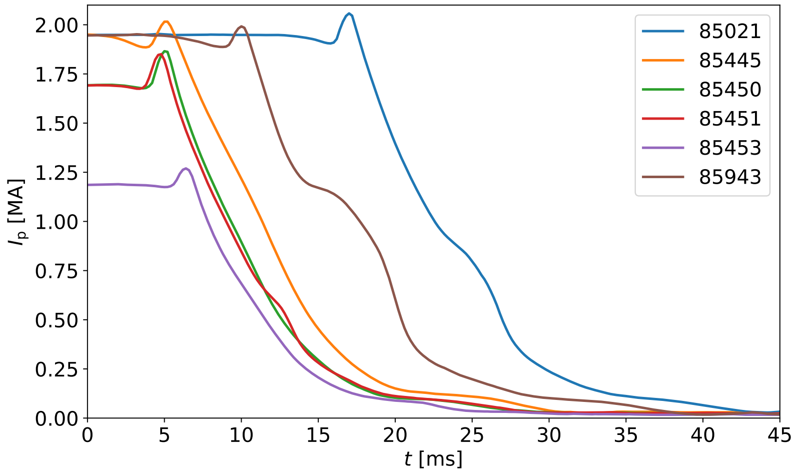

Figure 4.2: Plasma current evolution for each of the six used discharges. Note that the time axis is only relative, and serves mainly to give an understanding of the time interval for a disruption. What happens before the TQ is related to the startup of a disruption experiment in JET.

on the electron temperature T_e evolution experimental data for discharge #85943, shown in figure 2 of Nardon et al., 2021. The temperature exhibits a significant and rapid drop, the defining characteristic of the TQ phase, as the plasma current begins to decline before the spike in the current. The duration of this temperature drop is approximately 1 ms. The TQ is assumed to end (and the CQ start) right after the plasma current reaches its peak, at which point the temperature has stabilized to an essentially constant value.

Second, we define the end of the CQ phase to be the point in time when the RE current carries all of the plasma current, and the Ohmic current has decayed to practically zero. To determine this point, we examine the current evolution data for discharge #85943 (brown line), which exhibits a “bump” or a plateau in the middle of the current drop (at $\sim$ 16 ms in the figure). According to Nardon et al., 2021, this feature represents a short I_p-plateau, resulting from the increasing RE current during the CQ phase. This point should be where the Ohmic current becomes negligible, and the runaway current reaches its maximum. Moreover, the total current drop in experiment is supposedly due to a loss of REs. Our simulations do not model this late loss process, so wherever the bump appeared in these curves the simulations would show a plateau. Therefore, we assume that the middle of the bump signifies the end of the CQ and the beginning of the runaway plateau. For the other discharges, the time at which the RE plateau is reached is less distinct. Discharge #85943 exhibits the clearest bump in the plasma current among the used discharges. Therefore, we use discharge #85943 as a baseline working point for the parameter scans, noting that only one discharge is necessary to execute our scans.

A consequence of the choice of discharge is that we do not replicate the RE current magnitudes shown in figure 4.1. By inspecting figure 4.2, and given the assumption of where the runaway plateau begins, we will obtain a maximum RE current of about 1.15 MA, which is an order of magnitude larger than the 300 kA (the 3 T and Ar fraction = 1 case in figure 4.1) reported by Reux et al., 2015. It is therefore clear that Reux et al., 2015 has defined the runaway plateau in a different way compared to us. Whatever event occurs in the data after the RE plateau has been reached, which rapidly dissipates a large fraction of the RE current, our model is unable to capture. Moreover, if we pretended that the bump does not exist and instead assumed a linear decline of the plasma current down to 300 kA, it was difficult to match the CQ duration t_CQ in DREAM with that observed in experiments. For example, the simulations would then consistently underestimate t_CQ by several milliseconds.

4.2 Modelling disruptions in DREAM

Our disruption simulations comprised three distinct phases: initialization, transport window (TQ), and CQ. Although it is possible to simulate the subsequent runaway plateau phase, our focus was primarily on achieving the maximum runaway electron current, which typically occurred during the CQ simulation under our conditions. Therefore, the plateau phase was not explicitly modelled in our study. Each simulation stage inherits the parameters from the end of the previous stage (except for the initialization), unless specifically modified for the new simulation phase.

4.2.1 Initialization simulation

The initialization simulation sets the appropriate initial plasma parameters, such as the current density profile j and electric field E. Additionally, this phase initializes a complete Ohmic plasma, upon which the disruption proceeds. This phase runs for a single time step and is therefore only meant to be a setup for the coming simulation phases.

4.2.2 TQ and CQ simulations

Following the initial setup, the simulation proceeds to the TQ phase, which is characterized by a significant drop in plasma temperature. Several modelling decisions made for this phase are important for obtaining a realistic disruption evolution. The final phase of the simulation is the CQ, characterized by a drop in the Ohmic current and a rise in the runaway current. The TQ and CQ phases allow the plasma parameters to evolve self-consistently based on the dynamics described in the preceding chapter.

The simulations model the impact of magnetic perturbations, which occur when magnetic flux surfaces break up during the transport window, by defining the transport of runaway electrons and thermal energy. The quantities which experience this transport are the RE density n_{RE}, the cold electron temperature T_{cold}, and the distribution function of hot electrons f_{hot}. In our simulations, the magnitude of the magnetic perturbation $\delta B/B$ is considered a free parameter, assumed to be constant in both space and time coordinates during the transport window. However, since it is a free parameter, its value range is part of four conducted parameter scans. The effects of magnetic perturbations last during the full transport window duration t_{TQ}. Upon transitioning to the CQ phase, the simulation deactivates the magnetic perturbations, based on the assumption that the magnetic flux surfaces have reformed by this stage. However, to avoid the formation of non-physical hot Ohmic channels, a small value of $\delta B/B = 0.04\%$ is used for the heat transport (Pusztai et al., 2023).

The duration of the transport window t_{TQ} plays an important role in our model as it determines the period during which electron heat transport and RE transport are active. Furthermore, t_{TQ} is also treated as a free parameter. We opt for a transport window duration in the range of 0.075 ms to 0.15 ms, loosely based on the analysis by Björk et al., 2021[1]. For the subsequent CQ simulation a duration of

---

[1] Björk et al., 2021 used a τ_{TQ} parameter (denominator of the exponential function in (2.29), which is not the same as the transport window duration parameter in our work) in the range of 0.075 ms to 0.15 ms. If one assumes that the transport window lasts until the plasma temperature drops to approximately 100 eV from the initial 2541 eV of discharge #85943, the transport event duration t_{TQ} would be on the order of 0.5 ms. However, when using this time scale in our simulations, the RE current is severely underestimated. The energy dissipates for too long, and excessive transport of REs lead to a negligible amount of heat and REs at the start of the CQ simulation. This in

30 ms is used, which ensures a sufficient amount of time for the runaway current to stabilize in the simulation.

In our simulations, we assume that there is no initial population of REs. This means that any emergence of REs has to stem from the dynamics described by the RE generation mechanisms in place, specifically the Dreicer, hot-tail and avalanche mechanisms. Moreover, the investigated JET discharges were part of non-activated plasma operation, meaning that the tritium decay and Compton scattering generation mechanisms are not active. Furthermore, we assume the tokamak wall radius to be $1.5a$, where a is the minor radius. This is the effective wall radius of the first toroidally closed conducting structure and not the first wall. Therefore, the wall radius is more of a boundary condition for the electric field evolution. Radii within the range of a to $2a$ were explored, and we observed that while variations in the wall radius impacted the smoothness of the plasma current curve during the CQ simulation, they did not significantly affect the magnitude of currents or their rates of change $\mathrm{d}I_\mathrm{p}/\mathrm{d}t$. More accurately estimating the effective wall radius of JET would require additional data and thus falls beyond the scope of this thesis.

The transport window simulations uses the adaptive time stepper of DREAM, where the time step starts at 10^{-13} s, with an upper limit set to 10^{-4} s. For the CQ simulations, a fixed time step of 10^{-4} s is employed. Importantly, the choice of time step influences both the accuracy of the results and the computational cost. Smaller time steps may increase the accuracy of the data, but also require higher computational power. Conversely, larger time steps reduce computational cost but introduce a greater risk of numerical instabilities and reduced numerical accuracy, which can potentially skew the results. Thus, balancing accuracy and computational efficiency while also preventing numerical instabilities are important considerations throughout our simulations. Given that some parameter scans lasted nearly a full day under the chosen settings, further reducing the time step to enhance detail was deemed impractical due to the significant increase in computational demand and time constraints of the thesis work.

---

turn leads to the avalanche mechanism not generating any significant amount of REs, and as such results in an unrealistic disruption evolution.

5

Results and discussion

Having introduced the necessary theory in chapter 2, the numerical framework DREAM in chapter 3 and the method in chapter 4, we are now in position to study the RE existence conditions in JET discharges triggered by MGI of argon and deuterium. The primary goal of this study is the investigation of how the maximum RE current depends on magnetic field strength, initial plasma current and injected argon to deuterium ratio. Parameter scans over poorly constrained parameters are conducted to find regions in the magnetic perturbation strength $\delta B/B$, assimilation fraction f_i and transport window duration t_{TQ} parameter space, where the maximum RE current matches the measured current evolution data of discharge #85943 4.1.2. Furthermore, using this particular discharge together with a suitable set of parameter values (for the free parameters) as a baseline working point we perform parameter scans of the dependence of the maximum RE current on magnetic field strength, initial plasma current and injected argon to deuterium ratio. The results are compared with the results of the analysis by Reux et al., 2015 to see if similar trends in the RE current can be identified. The main purpose of this work is to attempt to reproduce figure 4.1, which shows the RE current as a function of toroidal magnetic field strength and injected argon to deuterium ratio. The disruption model we use is the one we described in chapters 3 and 4.

Section 5.1 presents the results for four different parameter scans of magnetic perturbation strength versus assimilation fractions, each scan conducted with a unique transport window duration. In section 5.2, we present the analysis of the plasma current matching, required for the subsequent parameter scans. In section 5.3, we present a parameter scan of the relationship between magnetic field strength B, injected argon fraction and maximum RE current. Moreover, a scan analyzing the effects of initial plasma current and argon fraction on the RE current is presented. Last, section 5.4 presents the same type of parameter scans as in section 5.3, except that in this case the argon injection profile is peaking outward, the details of which will be described in the section.

5.1 Magnetic perturbation strength versus assimilation fraction parameter scans

This section presents the parameter scans of the maximum RE current as a function of $\delta B/B$, assimilation fraction and transport window duration t_{TQ} for JET discharge #85943, which is our chosen baseline discharge. The scans are performed using a

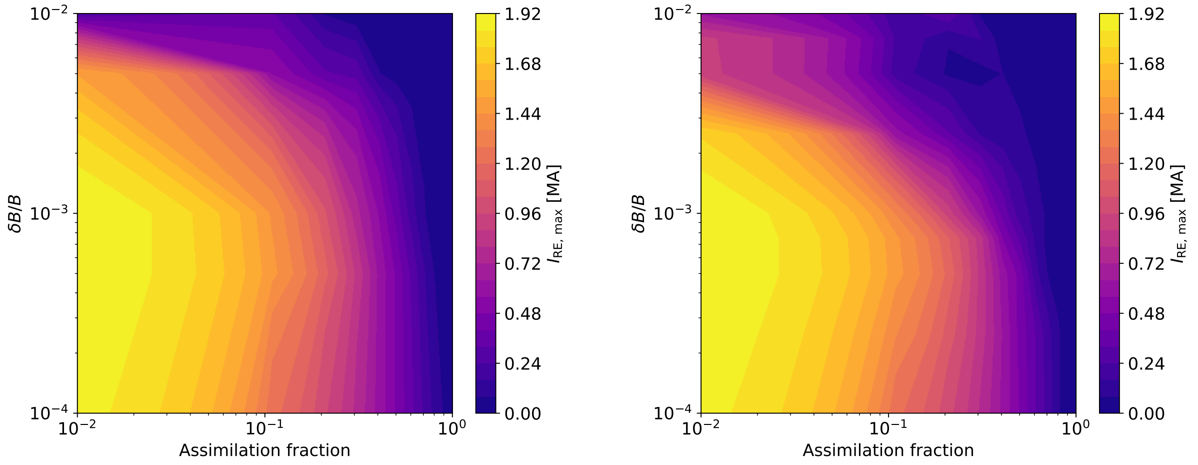

(a) $t_{\mathrm{TQ}} = 0.075$ ms. **(b)** $t_{\mathrm{TQ}} = 0.1$ ms.

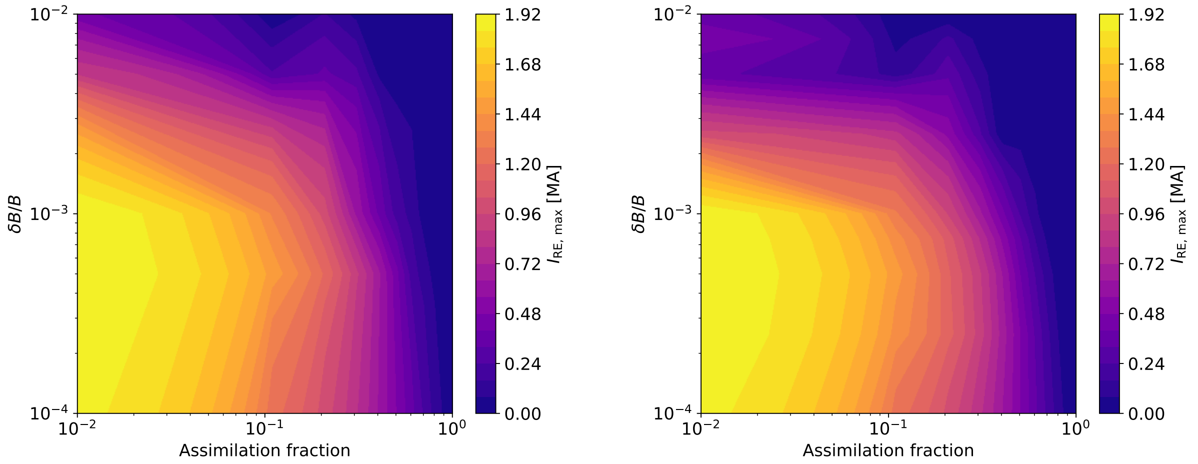

(c) $t_{\mathrm{TQ}} = 0.125$ ms. **(d)** $t_{\mathrm{TQ}} = 0.15$ ms.

Figure 5.1: Figures displaying $I_{\mathrm{RE,\,max}}$ as a function of $\delta B/B$ and assimilation fraction (f_i) for four different transport window (TQ) durations t_{TQ}, using JET discharge #85943 as a baseline discharge.

uniform injection profile, which means that all impurities are injected uniformly and instantaneously into the plasma. This assumption holds also for all the parameter scans in the coming sections, except for the scans presented in section 5.4, and this distinction will play a very important role later on.

We explore $\delta B/B$ values ranging from 10^{-4} to 10^{-2}, assimilation fractions from 1% to 100% and transport window durations between 0.075 ms to 0.15 ms. Each parameter scan consists of ten evenly distributed data points for $\delta B/B$ and ten for f_i, giving a total of 100 simulations per parameter scan. For each scan, the transport window duration is prescribed a constant value. Note that all our parameter scans (including all of the scans to come in the later sections) consist of the type of grid of data points just described. Moving on to the results, figure 5.1 shows two trends in the maximum RE current across all four thermal quench durations.

Firstly, the maximum RE current is non-monotonic. It increases with $\delta B/B$ for lower values of $\delta B/B$, then it decreases for higher values. The current peaks in the broad vicinity of $\delta B/B = 10^{-3}$ and an assimilation fraction near zero. Moreover, the current region close to $\delta B/B = 10^{-3}$ is where the maximum RE current is strongest for all the scanned assimilation values. The decrease in RE current magnitude for higher values of $\delta B/B$ is reasonable since more REs will be transported away if the magnetic perturbation strength is stronger.

Furthermore, as the transport window duration increases the upper part of the RE current landscape ($\delta B/B > 10^{-3}$) exhibits a significant reduction in RE current. This behaviour is quite expected because a longer transport window implies that the effects of transport are active for a longer period of time, thereby reducing the necessary transport strength to remove the same amount of REs and heat. Thus, transport intensity is being traded for the length of the transport window. In essence, increased transport duration inherently implies that fewer REs will be available to trigger the avalanche mechanism, hence reducing the maximum RE current.

Secondly, there is an almost linear decline in maximum RE current as the assimilation fraction increases, although this trend becomes less pronounced at the highest transport values (where the RE current is small anyway). This behaviour is somewhat unexpected, as it would be more intuitive for the RE current to increase with higher impurity levels due to a stronger cooling effect and consequently a stronger induced electric field, which would typically lead to an increased RE generation. We will however postpone the discussion of the observed dependence on argon to section 5.3.2.

The parameter scans indicate that multiple parameter setups can produce a maximum RE current of around 1.15 MA, which is the value at the end of the CQ in the current evolution data of figure 4.2. However as it turns out, not all parameter configurations successfully replicate the experimentally observed current quench durations—with there being deviations in the duration in the simulations of around 1 ms too long or short compared to the data. Nonetheless, we were able to identify a set of parameter values for the free parameters that lead to a match between the experimentally observed current evolution and simulated current evolution.

5.2 Plasma current evolution matching

This section details the method and results of the plasma current evolution matching between experimentally observed plasma current by Reux et al., 2015 and simulated plasma current for JET discharge #85943.

5.2.1 Setup

To replicate the current evolution observed in the analysis by Reux et al., 2015, we analyze how the plasma current I_p, its rate of change $\mathrm{d}I_\mathrm{p}/\mathrm{d}t$, and the duration of the CQ phase t_CQ are affected by the free parameters $\delta B/B$, assimilation fraction and transport window duration. Our results are compared to the data shown in figure 4.2. Additionally, we aim to make the maximum simulated RE current consistent with the total current evolution in experiment $I_\mathrm{p,\,exp}$ at the end of the CQ, as described in section 4.1.2.

Our method primarily involved a manual parameter search, which was deemed appropriate for our objective of detecting similar trends in the RE current between simulation and experimental analysis. Through iterative adjustment of parameters, we were able to match the currents. We aimed for the Ohmic current to be less than 100 kA, approximately 8% of $I_\mathrm{p,\,exp.}$, at the point where the experimental plasma current reaches the I_p-plateau. The identified best parameter setup for the chosen discharge is subsequently used as a baseline working point for upcoming parameter scans.

We rely on the results from the $\delta B/B$ versus assimilation fraction scans, as well as insights from prior studies such as Björk et al., 2021, Vallhagen et al., 2024, and Reux et al., 2015, to determine an adequate parameter setup. Applying the full experimental range of magnetic perturbations ($\delta B/B = 2\% - 16\%$), as plotted in figure 4 in Reux et al., 2015, severely underestimates the RE current, regardless of the other parameter values. Our parameter scans suggests that a significantly lower value of $\delta B/B \sim 0.1\%$ is more appropriate. The suitability of this order of magnitude is supported by Vallhagen et al., 2024, who computed $\delta B/B$ values in the range of 0.1 to 1% for ITER simulations using DREAM. An adequate magnetic perturbation value is identified to be $\delta B/B = 0.15\%$. Additionally, an assimilation fraction of $f_i = 10\%$ produces a realistic current evolution[1]. Lastly, based on the parameter scans, we find that $t_\mathrm{TQ} = 0.1$ ms yields a realistic current evolution when combined with the two other parameter values.

5.2.2 Matching

Figure 5.2 shows the plasma current $I_\mathrm{p,\,sim}$ (blue line), the Ohmic current I_Ω (green dash-dotted line), and the RE current I_RE (red dashed line) from the simulation, along with $I_\mathrm{p,\,exp}$ (brown line) from experimental analysis, during the CQ phase and the start of the runaway plateau (note that after $t = 5$ ms, i.e. right after the plateau of the bump, $I_\mathrm{p,\,exp}$ experiences another drop in magnitude, as also depicted in figure 4.2, which our model is unable to capture). Our disruption model is unable to replicate the spike in $I_\mathrm{p,\,exp}$[2] observed experimentally, so instead we as-

---

[1] Note that this could be related to the limitation that we assume spatially homogeneous transport levels that might not be representative of reality. We do this to keep the model simple such that we do no introduce further weakly constrained parameters.

[2] The current spike could potentially be modelled by enabling hyper-resistivity in DREAM, which leads to current density relaxation. However, this was deemed non-essential for this study

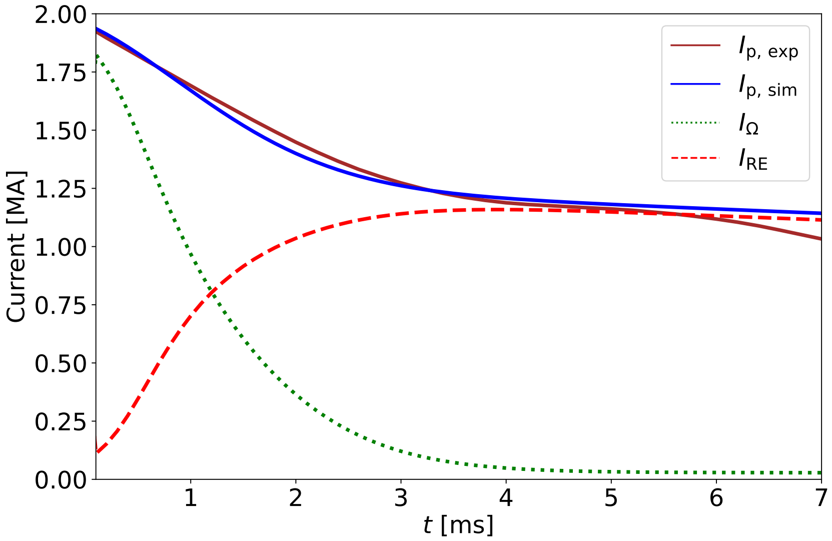

Figure 5.2: Plasma current I_p from experimental measurements and simulation during the CQ phase and the beginning of the runaway plateau. The figure also illustrates the simulated Ohmic current I_Ω and RE current I_RE.

sume that the CQ phase begins as this spike starts to decline at 1.9 MA (see figure 4.2). In the TQ simulation, $I_{\mathrm{p,\,sim.}}$ decays linearly from an initial 1.95 MA to 1.9 MA.

In figure 5.2, we observe that the RE current reaches its maximum value of approximately 1.15 MA after about 4.2 ms from the start of the TQ. Beyond this point, all currents gradually decline throughout the plateau phase, with the experimental current exhibiting a more rapid decrease. There is some discrepancy in the rate of change of the plasma currents, $\mathrm{d}I_\mathrm{p}/\mathrm{d}t$. Specifically, the DREAM model shows a steeper decay from 0 ms to 2 ms, followed by a gentler slope before becoming parallel with $I_{\mathrm{p,exp.}}$ at the end of the CQ phase. In contrast, $I_{\mathrm{p,\,exp.}}$ appears almost linear from 0 ms to 2.5 ms, before flattening out more at $t = 4.2$ ms. This difference may be because we opt for an adequate parameter setup, while an optimal setup may produce an even more exact matching. Still, the used setup is more than sufficiently good to be used as a baseline working point to carry out the remaining parameter scans.

Interestingly, varying the assimilation fraction has minimal impact on $\mathrm{d}I_\mathrm{p}/\mathrm{d}t$, resulting in only minor changes to the CQ duration. For instance, doubling or halving the assimilation fraction from the setup value altered t_CQ by less than 0.3 ms (approximately a 7% deviation from 4.2 ms). One might have expected that increasing (decreasing) the assimilation fraction would result in a quicker (slower) plasma current drop because the conductivity should directly determine the current decay rate, and the conductivity is highly sensitive to both the temperature and plasma Z_eff. However, it is possible that the final temperature (and thus t_CQ) is not very sensitive

---

and was omitted to avoid introducing additional free parameters.

to the concentration. This occurs if the radiated losses P_{rad} increase very rapidly as a function of temperature within a certain temperature range. The steady state is determined by the intersection of the $P_{\text{rad}}(T)$ and Ohmic heating $P_{\text{Ohm}}(T)$ curves. Increasing the argon content shifts the $P_{\text{rad}}(T)$ curve upwards, but this does not necessarily change the solution temperature.

Instead, the RE current magnitude changed noticeably when varying the assimilation fraction. Doubling the current resulted in an approximately 20% decrease in the maximum RE current, while halving it led to an $\sim$ 10% increase from the 1.15 MA observed in the baseline setup. This indicates a high sensitivity of the RE current magnitude to the assimilation parameter. This sensitivity is also evident in the $\delta B/B$ versus assimilation two-dimensional parameter scans, shown in figure 5.1.

5.3 Uniform Ar injection profile

The following sections present the results for two parameter scans of the maximum RE current when using the uniform injection profile for argon. This means that the injected argon and deuterium is injected uniformly and instantaneously into the plasma at the onset of the disruption simulation. The importance of this profile distinction will become more apparent later on, in section 5.4.

5.3.1 Magnetic field strength versus Ar fraction parameter scan

This section details the findings from a parameter scan of the maximum RE current $I_{\text{RE, max}}$ as a function of the magnetic field strength and argon fraction, which is the same type of analysis as figure 2 in Reux et al., 2015 (or figure 4.1 in section 4.1.1). The scan is conducted with the equilibrium of JET discharge #85943 along with the parameter setup $\delta B/B = 0.15\%$, $f_i = 10\%$ and $t_{\text{TQ}} = 0.1$ ms. For each simulation, the magnetic field strength B of the chosen discharge is re-scaled by a factor C_B, while the initial plasma current $I_{\text{p, 0}}$ and field line geometry is held fixed (i.e. the poloidal and toroidal field components are scaled together). Recall that the baseline case has a field strength of 3 T, implying that $C_B = 0.5$ gives $B_{C_B} = 1.5$ T. The argon fraction parameter represents the fraction of injected argon in relation to the total amount of injected particles (argon and deuterium). The total number of injected atoms is the same across all simulations. Note again that the initial plasma current is not varied with the magnetic field self-consistently. This choice enables us to disentangle the parameter dependencies, allowing us to analyze how each individual parameter affects the RE current.

Figure 5.3 shows the result. For a given field strength, a distinct trend is observed where the maximum RE current decreases with increasing argon fraction, where the current peaks at an argon fraction of 0.1 and drops to negligible values at an argon fraction of 0. The argon dependence is discussed in the next section.

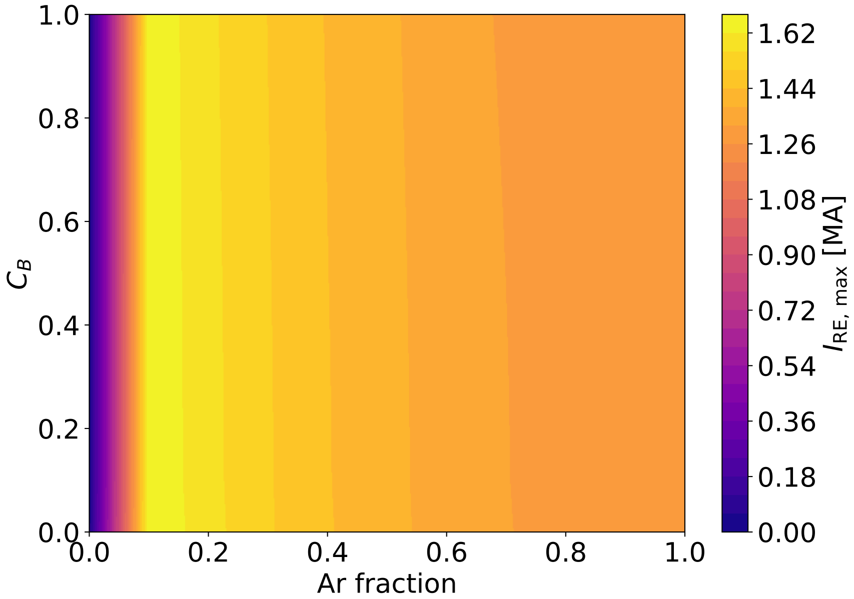

Figure 5.3: $I_{\mathrm{RE,\ max}}$ as a function of baseline magnetic field strength $B = 3$ T scaled by C_B and Ar fraction. Note that the plasma current is not re-scaled consistently with B.

Moreover, the RE current appears to only have a very weak dependence on the magnetic field strength across most of the scanned range. This is not too unreasonable, as the primary role of the magnetic field in a tokamak is to confine the plasma and maintain stability. Unless there are drastic changes in the magnetic field that lead to a loss of confinement or major shifts in plasma stability, such as magnetohydrodynamics (MHD) instabilities, variations in the field strength do not directly impact runaway current generation. Instead, the generation of REs is more directly related to the electric field.

The weak dependence on the magnetic field strength still seen, specifically the RE currents slight decrease with increasing field strength, may be attributed to the critical momentum p_c, which depends on the magnetic field strength through synchrotron losses. According to equation (3.12) the gyration frequency of electrons depends on the magnetic field strength. As the field strength increases the gyration frequency also increases, resulting in greater energy dissipation due to synchrotron radiation. Consequently, electrons require more energy to become runaway electrons, leading to an increase in the critical momentum, and hence a slightly reduced RE current.

Interestingly, in figure 5.3 the RE domain boundary is entirely vertical, in contrast to the green RE domain boundary in figure 4.1. However, one important distinction between the analysis of Reux et al., 2015 and our simulations is that we only re-scale B, whereas in Reux et al., 2015 both B and I_p were re-scaled proportionally to maintain a similar safety factor. The safety factor in tokamaks is a measure of the twist of the magnetic field lines, defined as the ratio of toroidal to poloidal field line lengths. Another difference between the models is that our model uses a single discharge as a baseline working point, characterized by a specific set of initial conditions for temperature, electron density, initial plasma current, and magnetic geometry. In contrast, in the analysis by Reux et al., 2015, each data point corresponds to an individual discharge, exhibiting variations in several input parameters. To evaluate our ability to more accurately reproduce the green domain boundary, we will vary $I_{\mathrm{p},0}$ while maintaining a constant magnetic field strength.

5.3.2 Initial plasma current versus Ar fraction parameter scan

The next parameter scan concerns the maximum RE current as a function of the initial plasma current $I_{\mathrm{p},0}$ and argon fraction. This time the initial plasma current is scaled by a factor C_{I_p} unique to each simulation, similar to how the magnetic field strength is re-scaled by C_B in the the magnetic scans in the previous section. Note that in this parameter scan, the magnetic field strength B is held fixed.

In figure 5.4, we not only see a strong dependence on the argon fraction for the maximum RE current, which was the strongest dependence we observed in the parameter scan in the previous section, we also notice a strong dependence on the C_{I_p}-factor. A high C_{I_p}-factor increases I_{RE}, reaching a peak of approximately 1.62 MA around an argon fraction of 0.05. The trend of increasing RE current with increasing C_{I_p} is reasonable since a stronger initial plasma current will inherently scale the induced electric field and thus the generated runaway current. Additionally, the avalanche gain is exponentially sensitive to $I_{\mathrm{p},0}$.

However, the observed increase in I_{RE} with a decrease in argon fraction is particularly interesting. Moving to the right of a 0.05 argon fraction, while fixing C_{I_p}, we observe a decrease in the RE current maximum, for all the C_{I_p}-factor values, eventually reaching the baseline case value of 1.15 MA at $C_{I_\mathrm{p}} = 1$ and an argon fraction of 1. To attempt to understand this behaviour, we investigate the roles of argon and deuterium by analyzing two unique cases. We may call these cases: Case A, characterized by a C_{I_p}-factor of 1 and an argon fraction of 0.2 (deuterium fraction = 0.8), and Case B, with the same C_{I_p}-factor but an argon fraction of 0.8 (deuterium fraction = 0.2).

Analysis of the RE current densities during the CQ phase, as depicted in figure 5.5 (left), reveals at least two interesting differences. In Case A, the current density is larger over a broader section of the plasma cross-section, approaching zero at the plasma edge. Meanwhile, in Case B, the current density approaches zero approximately 0.1 m earlier, while the peak density value is higher near the plasma centre compared to Case A. However, this higher peak density does not directly translate into a higher runaway current I_{RE}, because I_{RE} is derived from integrating the current density across the entire cross-section.

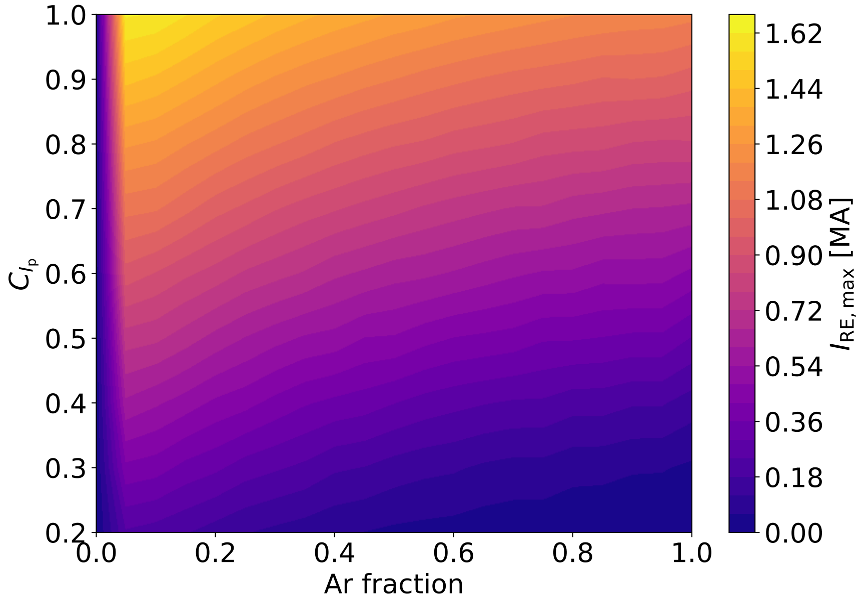

Figure 5.4: $I_{\mathrm{RE,\,max}}$ as a function of the initial plasma current scale factor C_{I_p} and Ar fraction for the uniform argon injection profile.

To understand the differences in j_{RE} between the two cases we link it to the F_{hot} runaway generation mechanism, which we recall is the flux of runaways through the upper boundary of the hot momentum grid (sum of the primary generation mechanisms), the electric field and temperature. We also recall that the electric field in the plasma is induced by changes in conductivity σ, according to Ohm's law. Since σ is proportional to $T^{3/2}$ (see equation (2.21)), a drop in temperature results in decreased conductivity and thus a stronger induced electric field. Figure 5.5 (right) illustrates the energy density $W_{\mathrm{cold}} + E_{\mathrm{k},\,f_{\mathrm{hot}}}$, which is proportional to the plasma temperature, at the plasma centre. We observe that the thermal energy decreases more rapidly in Case B, which is due to more effective energy dissipation through radiation. In contrast to argon, the injected deuterium simply redistributes energy within the plasma.

Hot-tail generation depends on the rate of temperature decrease, where a faster temperature decline results in an increase of hot-tail generation. This is because a significant number of electrons remain in the high-energy tail of the Maxwell distribution, thereby increasing their probability of achieving the energy necessary to exceed the critical threshold for RE formation. Essentially, a faster cooling rate provides more time for high-energy electrons to be accelerated by the plasma's electric fields before they cool below the threshold for RE generation. This phenomenon is observed in Case B, where significant hot-tail initiates earlier compared to Case A, as seen in figure 5.6.

However, an important factor for the maximum RE current trend could also be the ratio $E/E_{\mathrm{c,\,eff}}$, which is in fact greater in Case A compared to Case B, during the onset of the CQ as seen in figure 5.7 (right). This difference arises because Case

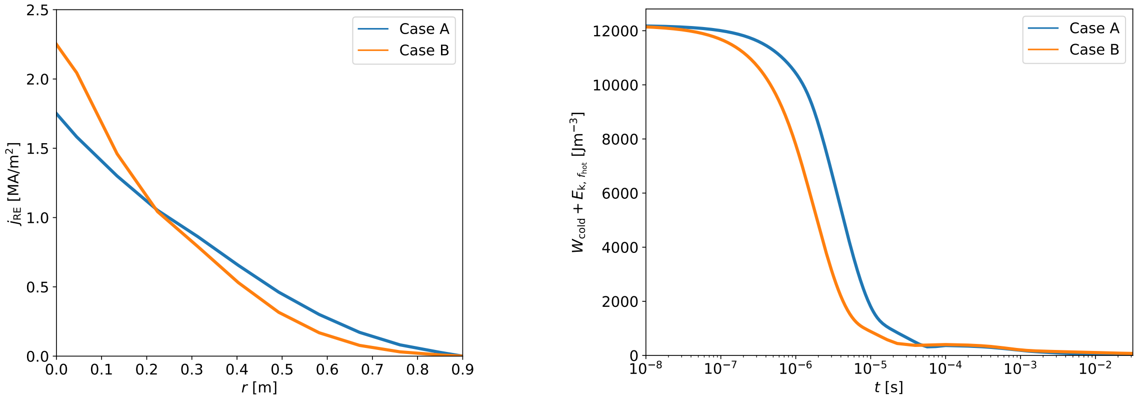

Figure 5.5: (Left) RE current density j_{RE} 2 ms after the onset of the TQ. (Right) Energy density $W_{\mathrm{cold}} + E_{\mathrm{k},\, f_{\mathrm{hot}}}$ at the plasma centre.

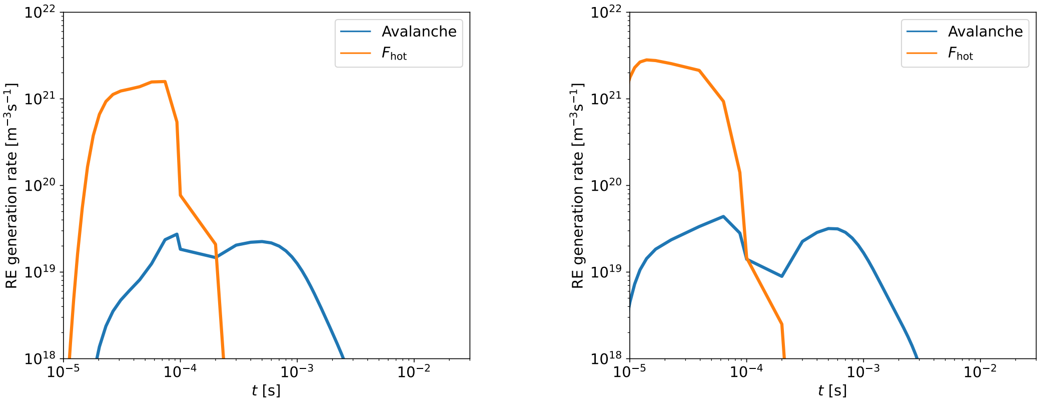

Figure 5.6: RE generation rates at the plasma centre for case A (left) and case B (right).

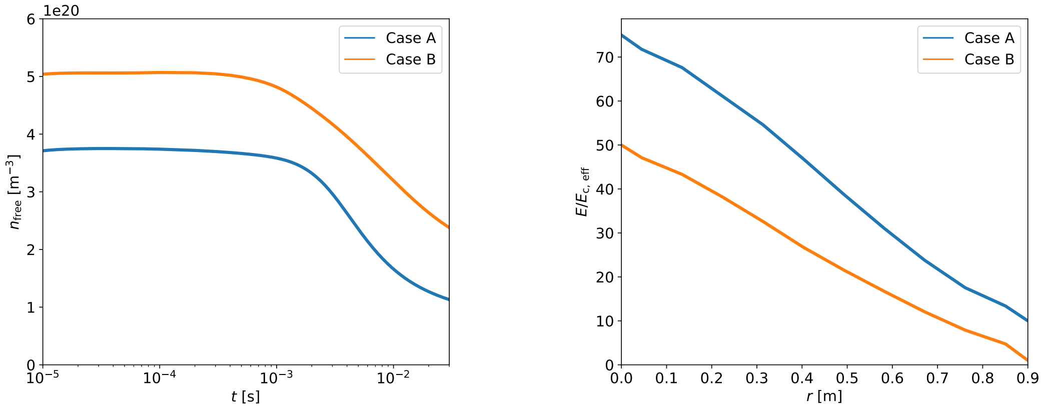

Figure 5.7: (Left) Free electron density n_{free} at the plasma centre. (Right) Electric field ratio $E/E_{\mathrm{c,\,eff}}$ at the onset of the CQ (0.2 ms after the onset of the TQ).

B, with its higher argon fraction, has a higher electron concentration, leading to a larger effective critical electric field (see equation (2.28)). The total electron density n_{tot} in Case B is approximately 3.5 times that of Case A. Additionally, the density of free electrons is also greater in Case B throughout the simulation, which is shown in figure 5.7 (left). In Case B, where the effective critical electric field $E_{\mathrm{c,\,eff}}$ is about three times larger, the reduced $E/E_{\mathrm{c,\,eff}}$ ratio likely results in fewer electrons transitioning to runaway electrons compared to Case A.

It is intriguing that we observe a decrease in the RE current with an increased argon fraction. Intuitively, one would expect that the increased radiation from larger impurity amounts and consequently a stronger induced electric field would be the dominant effect on the runaway current. To investigate if we could reproduce the argon dependence seen in figure 4.1 and potentially also match the green runaway domain boundary, we now introduce an additional layer of complexity into our model.

5.4 Edge-peaked Ar injection profile

The injection of argon and deuterium occurs at the onset of the TQ simulation, where the full impurity amount is assumed to enter the plasma immediately. The mixing efficiency is the fraction of atoms that are delivered to the plasma centre, and heavy impurity gases such as argon typically have poorer mixing efficiency with the plasma compared to light atoms such as deuterium (Bozhenkov et al., 2008; Reux et al., 2015).

To address this, an assumption is now made for argon's mixing behaviour. We model argon with a distinct radial profile to artificially emulate its actual mixing properties. This approach involves confining the injected argon to the plasma edge, where it remains as the system evolves, thus not letting it mix completely with the bulk plasma. This is realised by prescribing the radial profile

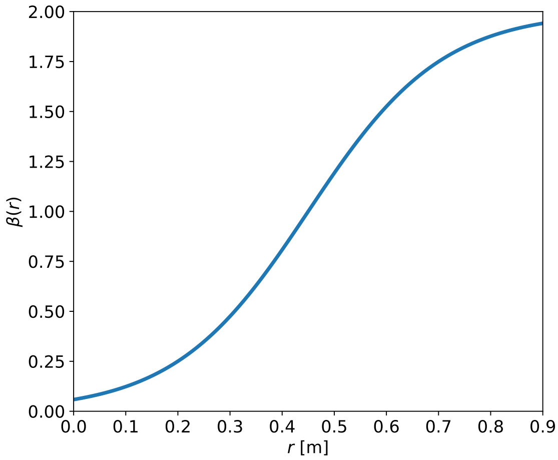

Figure 5.8: Edge-peaked radial profile (equation (5.1)).

$$\beta(r) = 1 + \tanh\left[c\left(\frac{r}{a} - 0.5\right)\right], \tag{5.1}$$

where $c = 3.5$ and a is the minor radius. This particular choice of c mimics the desired behaviour of argon under experimental conditions while maintaining good numerical stability in the simulations. Figure 5.8 illustrates this function. The injected argon density n_{Ar} (which is a constant) is multiplied by the edge-peak factor $\beta(r)$, resulting in the edge-peaked injection density

$$n_{\mathrm{Ar,\,edge}}(r) = \beta(r)\frac{\int_0^a V'\,\mathrm{d}r}{\int_0^a \beta(r)V'\,\mathrm{d}r} n_{\mathrm{Ar}} \tag{5.2}$$

The quotient of integrals acts as a normalization factor which ensures that the total number of atoms remains constant. In our work, argon is injected with either the edge-peaked profile or a uniform profile, while deuterium is always injected using a uniform profile. Note that a uniform profile is obtained when $c = 0$ in (5.1).

When also the different mixing efficiencies of argon and deuterium are considered, we observe a reversed behaviour in the maximum RE current in both our magnetic field versus argon fraction and initial plasma current versus argon fraction parameter scans, presented in sections 5.4.1 and 5.4.2 respectively. The new results are more consistent with experimental observations, highlighting the significance of mixing efficiency and the injection profile of the impurities. We now present these types of scans again, but when the edge-peaked argon injection profile is used. The parameter scans are otherwise conducted using the same parameter setup as in the uniform injection case, except that $\delta B/B = 0.2\%$ instead of $\delta B/B = 0.15\%$. This small adjustment is necessary to achieve a similar quality match for the current evolution as in figure 5.2.

5.4.1 Magnetic field strength versus Ar fraction parameter scan

Figure 5.9 illustrates the maximum RE current as a function of magnetic field strength and argon fraction. We observe a similar trend on the magnetic field dependence as in the uniform injection profile scan, namely that the RE current is only very weakly affected by the magnetic field strength. This dependence is still due to the critical momentum as discussed in section 5.3.1. However, we now observe an opposite behaviour regarding the argon fraction. The maximum RE current increases monotonically with the argon fraction, reaching its peak value for a pure argon case and dropping to negligible RE currents at an argon fraction of 0. This behaviour seems more reasonable, and the observed trend is partly in agreement with the analysis of Reux et al., 2015.

5.4.2 Initial plasma current versus Ar fraction parameter scan

Figure 5.10 shows the parameter scan of $I_{\mathrm{RE,\,max}}$ as a function of initial plasma current and argon fraction, where we observe a dependence of I_{RE} on both parameters. There is a trend of increasing I_{RE} for larger initial plasma current, regardless of the argon fraction value. The RE current reaches a maximum for the baseline working point, at $C_{I_{\mathrm{p}}} = 1$ and Ar fraction $= 1$. For $C_{I_{\mathrm{p}}}$-values less than 0.2, $I_{\mathrm{RE,\,max}}$ is essentially negligible. The effect of the plasma current is similar to the uniform injection case, and the reason for this behaviour has not changed.

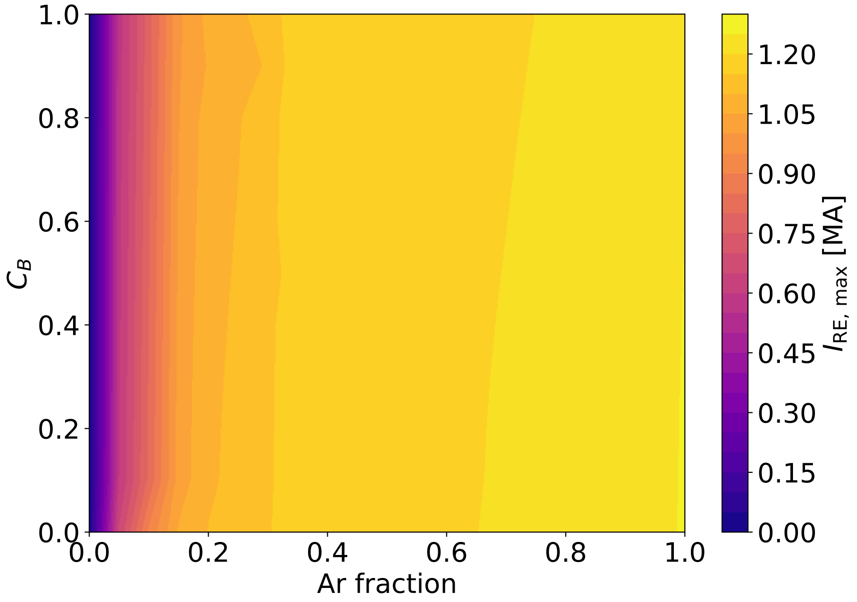

Figure 5.9: $I_{\mathrm{RE,\,max}}$ as a function of baseline magnetic field strength $B = 3$ T scaled by C_B and Ar fraction using the edge-peaked argon injection profile. Note that the initial plasma current is not re-scaled consistently with B.

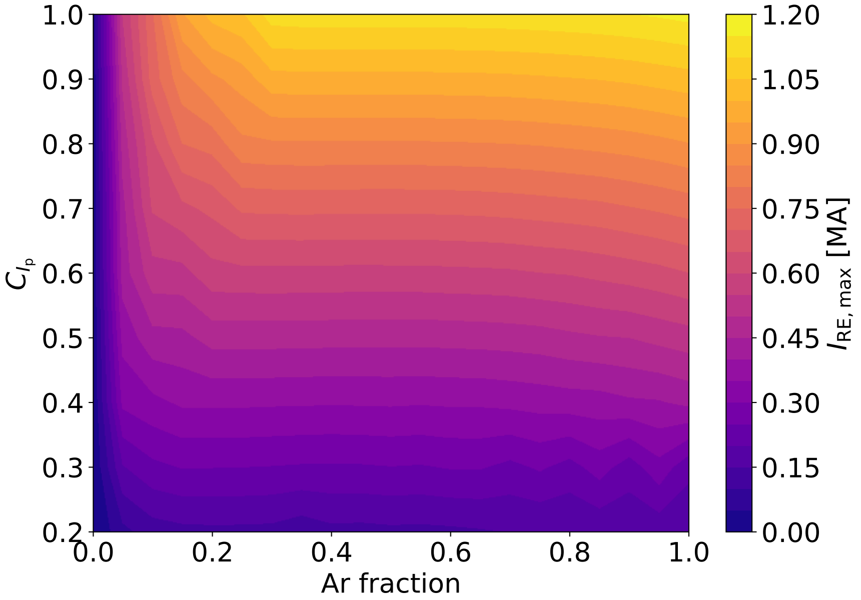

Figure 5.10: $I_{\mathrm{RE,\,max}}$ as a function of initial plasma current scale factor $C_{I_{\mathrm{p}}}$ and Ar fraction using the edge-peaked argon injection profile. Note that the magnetic field strength is not re-scaled consistently with $I_{\mathrm{p},0}$.

Furthermore, if we consider a given C_{I_p} we observe a trend of slight increase in $I_{\mathrm{RE,\,max}}$ with higher argon fractions, where the impact appears to be largest for either low (< 0.3) or high argon fractions (> 0.9). Meanwhile, minimal dependence on the argon fraction is observed in the range of fractions 0.3–0.65. We now discuss what factors primarily contribute to the observed dependence on argon.

First, the impact of argon on the plasma's electron density is an important factor to consider. Argon, with $Z = 18$, contributes a significantly larger number of free electrons when ionized compared to deuterium ($Z = 1$). Figure 5.11 shows the free electron density n_free at radius $r = 0.8$ m for simulations with $C_{I_\mathrm{p}} = 1$ and argon fractions of 0.9 and 0.3, respectively. The presence of the additional electrons in the case with an argon fraction of 0.9 is important because the large number of total electrons increases the friction force, making it less likely for electrons to run away. However, a large number of total electrons is beneficial for the avalanche mechanism as it increases the probability for large-angle collisions which can kick the electrons into the runaway region.

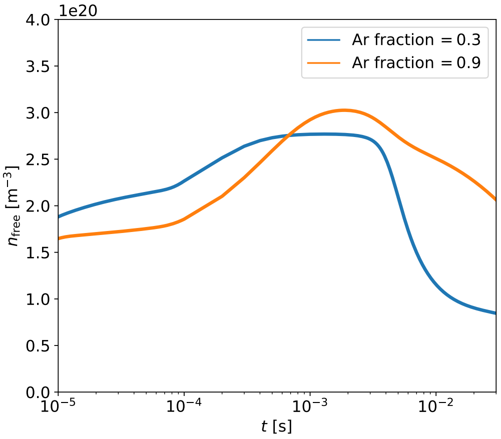

Figure 5.11: Free electron density n_free at radius $r = 0.8$ m.

Another factor to consider is the critical effective electric field $E_{\mathrm{c,\,eff}}$, which depends on the electron density (equation (2.28)). We observe that in a high deuterium case, the critical field is lower compared to a high argon case. This implies that in the former case, the energy required for electrons to become runaway is lower than in the latter case, assuming the electric field is equally strong in both cases. In fact, the ratio between the electric field and the effective critical field $E/E_{\mathrm{c,\,eff}}$ is larger in a high deuterium fraction case, as shown in figure 5.12 (right). This is consistent with Case A having larger electric field ratio compared to Case B in the uniform injection profile case, discussed in section 5.3.2. Despite the electric field being weaker in the Ar fraction $= 0.3$ scenario, we still observe a considerable amount of REs being generated.

Importantly, the increased amount of argon in the plasma gives rise to more radiative cooling, as argon ions radiate energy more efficiently than deuterium. This efficiency is due to argon's greater number of available electron transitions that can release photons compared to deuterium. The enhanced radiative cooling results in a significant drop in the overall plasma temperature, leading to a steeper temperature gradient within the plasma. Figure 5.12 (left) shows the energy density. The faster drop and reduced temperature in the high argon case induce a stronger electric field more quickly compared to the high deuterium case, thus generating more REs via the RE seed and avalanche. Figure 5.13 show the RE generation rates for the two analyzed cases. In the high argon case, we observe a stronger F_{hot} due to the enhanced cooling and also an avalanche that remains significant for a longer period of time (note the log-log scale).

These results show that our model is able to replicate experimental observations, where we see a similar dependence of $I_{\mathrm{RE,\,max}}$ on the argon fraction. Our model shows higher RE current magnitudes compared to the analysis of figure 4.1, but this discrepancy is due to our current matching, where we aimed for a baseline case with a maximum RE current of 1.15 MA. The bump for discharge #85943 shown in figure 4.2 signifies that additional events happen in experiment which our model is unable to capture. This is however perfectly normal and simply means we should not try to compare all RE current magnitudes and rather focus on the general RE current trends.

Both the simulation and experimental analysis show negligible RE current below $C_{I_{\mathrm{p}}} = 0.3$ in the simulation and below the corresponding $B = 1$ T in the experiments. Our results indicate a steep decline in RE current for argon fractions under 0.1, regardless of the initial plasma current. In the analysis by Reux et al., 2015, this region too shows no significant trace of RE current. In figure 4.1, the RE current is considered insignificant for Ar fractions < 0.2, and in figure 5.10 one can also see that the current starts to decline for Ar fraction < 0.2. Furthermore, at a toroidal field strength of approximately 1.5 T and an argon fraction of 1, the experimental analysis show a significant amount of runaway current, whereas our simulations suggest that the runaway current decreases linearly with the initial plasma current. Finally, the edge-peaked model better captures the runaway domain boundary observed in figure 4.1, where the RE current dependence on argon trend is fairly similar.

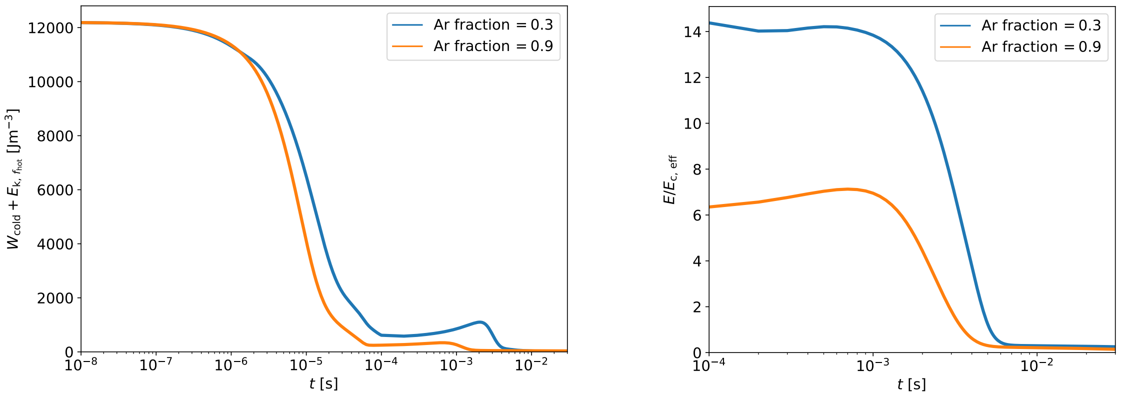

Figure 5.12: Energy density at the plasma centre (left) and $E/E_{\mathrm{c,\,eff}}$ at $r = 0.8$ m (right).

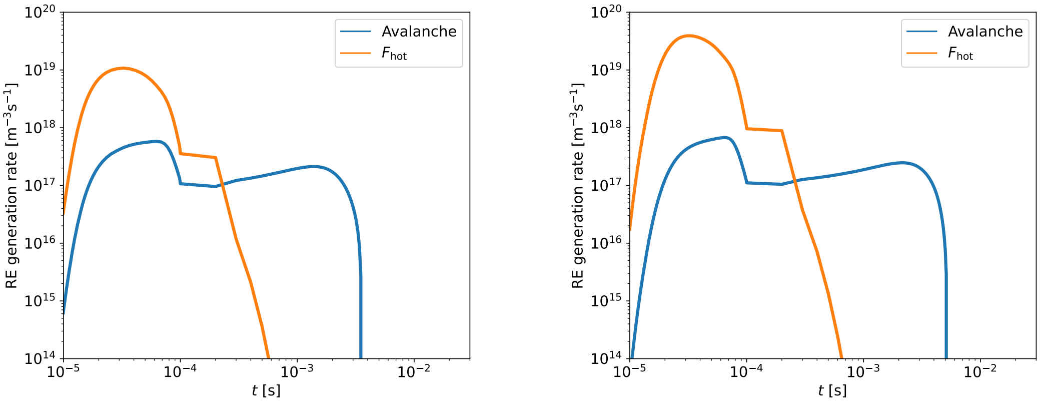

Figure 5.13: RE generation rates for the cases: Ar fraction $= 0.3$ (left) and Ar fraction $= 0.9$ (right) at radius $r = 0.8$ m.

6

Conclusions

This work has focused on the simulation of runaway electron (RE) dynamics during massive gas injection (MGI) disruptions in JET. Our study specifically investigated the conditions for runaway electron existence in JET, using a particular JET discharge as a baseline and comparing simulation results with the experimental analysis conducted by Reux et al., 2015. The simulations aimed at understanding the behaviour of REs under various tokamak operational conditions, including changes in magnetic field strength, initial plasma current, and the injected quantities of argon and deuterium.

The simulation results showed that RE current is sensitive to several parameters, including the injected argon to deuterium ratio and initial plasma current. Notably, the study demonstrated that an increase in the injected argon fraction leads to a rise in RE current if the argon density peaks towards the plasma edge. This type of density profile aimed to emulate the mixing properties of argon with the plasma. The observed trend arises primarily from the stronger cooling effect, due to the increased argon radiation, which leads to a stronger induced electric field, and, consequently, a more impactful avalanche. Also the electric field ratio $E/E_{\mathrm{c,\,eff}}$ appears to have a strong effect on the runaway current.

We have also made an attempt at reproducing the RE boundary for JET-ILW, seen in figure 2 of Reux et al., 2015 or figure 4.1 in section 4.1.1, through simulation. We find that the trend between the RE boundary of figure 2 in Reux et al., 2015 and the RE current in our figure 5.10 is fairly similar. Additionally, although figure 2 uses magnetic field strength to label each discharge, each B is also associated with a corresponding value of the initial plasma current. Our results show that it is primarily the variation in initial plasma current that significantly influences the RE dynamics.

Furthermore, higher initial plasma current (while keeping the magnetic field strength fixed) is found to increase the RE current, while higher magnetic field strength (with fixed initial plasma current) results in only a very small reduction of the RE current. The increase in RE current with higher initial plasma current arises because a stronger initial current inherently scales the induced electric field, thereby generating more runaway electrons via the avalanche mechanism. Conversely, the slight (barely noticeable) reduction in RE current with stronger magnetic fields may be attributed to the higher critical momentum required, making avalanche generation less efficient. This increase in p_{c} is due to the fact that synchrotron radiation losses increase with increasing magnetic field strength. As the magnetic field strength increases, the gyration frequency of the electrons also increases, leading to greater energy loss of the energetic electrons through synchrotron radiation.

6.1 Outlook

The results demonstrate that the simulation framework DREAM, employed in this work, can be effective in predicting and analyzing RE behaviour in JET disruptions. However, discrepancies in modelling the precise behaviour of each atomic element (deuterium and argon in our case) indicate areas where the model could be improved. For instance, the employed uniform and edge-peaked argon injection profiles may not perfectly capture the complex physical interactions present in experiments. Additionally, these profiles do not accurately represent the mixing process of the impurities and were primarily used as a simple model to account for this added complexity.

Based on our results, a significant improvement, and a natural next step, would be to simulate the gas injection more accurately. Our current model assumes that injected impurities enter the plasma instantaneously at the start of the simulation, which does not reflect reality. In practice, impurities gradually enter the plasma from the edge and distribute themselves over time. Developing or employing a more sophisticated model would not only improve simulation accuracy but could also contribute to theoretical advancements in MGI-theory.

Adding more complexity into the model has the potential to refine its accuracy. For example, we used spatially homogeneous heat and RE transport levels, which may not accurately reflect the actual conditions. This simplification is used to avoid introducing further weakly constrained parameters. However, a more complex transport model and model for impurity assimilation could also be beneficial. We assume that a fraction of the injected impurities are assimilated in the plasma. Furthermore, we treat the assimilation fraction of argon and deuterium to be the same to keep the model simple. However, an increased model complexity (unless the self-consistent aspect of the code is improved in some way) comes with more free parameters that are not well constrained experimentally. So it only makes sense to increase complexity if there is enough reliable empirical data to constrain these free parameters. Otherwise, the problem is ill-posed.

There are opportunities for improvement on the experimental side as well, since some parameters are not well constrained by current experiments, which contributes to uncertainty. This issue could be addressed by employing additional diagnostics and utilizing data from these tools to provide more detailed information about RE behaviour and overall plasma evolution during disruptions.

Another potential direction for future research is to replicate this exercise for a different tokamak or across multiple tokamaks. The primary goal of model validation is to ensure that the model performs reliably in all existing machines, thereby building confidence that it will also accurately predict results in future machines.

Finally, a promising area for future research is the integration of machine learning methods to improve the predictive capabilities of the disruption model. By training machine learning algorithms on large datasets from both simulations and experimental results, it may be possible to identify patterns and correlations that are not easily discernible through traditional methods. This approach could improve parameter estimation and reduce uncertainties in both parameters and data. Additionally, optimization methods could be utilized to more efficiently search for optimal parameter configurations, while also allowing for the exploration of a broader parameter space.

6.2 Final thoughts

The insights gained from this study will hopefully serve as a foundation for further research and development in fusion energy. From a practical standpoint, the ability to predict and mitigate the risks associated with REs, as well as understanding the impact of impurity injection and its role in controlling REs, is important for the development of future fusion reactors. The code validation in this project builds confidence that our models accurately describe the conditions in existing tokamaks, enabling their use in the design of future tokamaks.

Bibliography

Anderson, D., Mietek, L., Johannisson, P., & Marklund, M. (2008). *Basic plasma physics theory and applications.*

Andrei, M. (2019). UK wants to build world's first fusion power plant 20 years from now. https://www.zmescience.com/science/uk-wants-to-build-worlds-first-fusion-power-plant-20-years-from-now/

Bellan, P. (2008). *Fundamentals of plasma physics.* Cambridge University Press.

Björk, K. I., Vallhagen, O., Papp, G., Reux, C., Embreus, O., Rachlew, E., Fülöp, T., the ASDEX Upgrade Team, JET contributors, & the EUROfusion MST1 Team. (2021). Modelling of runaway electron dynamics during argon-induced disruptions in ASDEX Upgrade and JET. *Plasma Physics and Controlled Fusion*, *63*(8), 085021. https://doi.org/10.1088/1361-6587/ac07b5

Bozhenkov, S. A., Lehnen, M., Finken, K. H., Jakubowski, M. W., Wolf, R. C., Jaspers, R., Kantor, M., Marchuk, O. V., Uzgel, E., Wassenhove, G. V., Zimmermann, O., Reiter, D., & the TEXTOR team. (2008). Generation and suppression of runaway electrons in disruption mitigation experiments in TEXTOR. *Plasma Physics and Controlled Fusion*, *50*(10), 105007. https://doi.org/10.1088/0741-3335/50/10/105007

Breizman, B. N., Aleynikov, P., Hollmann, E. M., & Lehnen, M. (2019). Physics of runaway electrons in tokamaks. *Nuclear Fusion*, *59*(8). https://doi.org/10.1088/1741-4326/ab1822

Chen, F. F. (1974). *Introduction to plasma physics and controlled fusion.* Springer International Publishing.

Cohen, R. S., Spitzer, L., & Routly, P. M. (1950). The electrical conductivity of an ionized gas. *Phys. Rev.*, *80*, 230–238. https://doi.org/10.1103/PhysRev.80.230

Connor, J., & Hastie, R. (1975). Relativistic limitations on runaway electrons. *Nuclear Fusion*, *15*(3), 415. https://doi.org/10.1088/0029-5515/15/3/007

Creely, A. J., Greenwald, M. J., Ballinger, S. B., Brunner, D., Canik, J., Doody, J., Fülöp, T., Garnier, D. T., Granetz, R., Gray, T. K., & et al. (2020). Overview of the SPARC tokamak. *Journal of Plasma Physics*, *86*(5), 865860502. https://doi.org/10.1017/S0022377820001257

Crepaz, L. (2023). Pioneering JET delivers final plasma. https://ccfe.ukaea.uk/pioneering-jet-delivers-final-plasma/

Decker, J., Hirvijoki, E., Embreus, O., Peysson, Y., Stahl, A., Pusztai, I., & Fülöp, T. (2016). Numerical characterization of bump formation in the runaway electron tail. *Plasma Physics and Controlled Fusion*, *58*(2), 025016. https://doi.org/10.1088/0741-3335/58/2/025016

Dreicer, H. (1959). Electron and ion runaway in a fully ionized gas. i. *Phys. Rev.*, *115*, 238–249. https://doi.org/10.1103/PhysRev.115.238

Effenberg, F. (2022). Blowing dust to cool fusion plasmas. https://www.energy.gov/science/fes/articles/blowing-dust-cool-fusion-plasmas

Embréus, O., Stahl, A., & Fülöp, T. (2018). On the relativistic large-angle electron collision operator for runaway avalanches in plasmas. *Journal of Plasma Physics*, *84*. https://doi.org/10.1017/S002237781700099X

Energy.gov. (2023). DOE explains...Tokamaks. https://www.energy.gov/

EUROfusion. (2024). Breaking New Ground: JET Tokamak's Latest Fusion Energy Record Shows Mastery of Fusion Processes. https://euro-fusion.org/eurofusion-news/dte3record/

European Union. (2008). Design Specification. https://op.europa.eu/en/publication-detail/-/publication/cc7f776b-5261-4f34-b4de-3734ddf0624c/language-en

Fülöp, T., Helander, P., Vallhagen, O., Embreus, O., Hesslow, L., Svensson, P., Creely, A., Howard, N., & Rodriguez-Fernandez, P. (2020). Effect of plasma elongation on current dynamics during tokamak disruptions. *Journal of Plasma Physics*, *86*(1), 474860101. https://doi.org/10.1017/S002237782000001X

Greenwald, J. (2016). Major next steps for fusion energy based on the spherical tokamak design. https://web.archive.org/web/20210919050707/https://www.pppl.gov/news/2016/08/major-next-steps-fusion-energy-based-spherical-tokamak-design

Helander, P., Eriksson, L.-G., & Andersson, F. (2002). Runaway acceleration during magnetic reconnection in tokamaks. *Plasma Physics and Controlled Fusion*, *44*(12B), B247. https://doi.org/10.1088/0741-3335/44/12B/318

Helander, P., & Sigmar, D. J. (2005). *Collisional transport in magnetized plasmas*. Cambridge University Press.

Hender, T. C., et al. (2007). Chapter 3: MHD stability, operational limits and disruptions. *Nuclear Fusion*, *47*(6), S128. https://doi.org/10.1088/0029-5515/47/6/S03

Hirvijoki, E., Pusztai, I., Decker, J., Embréus, O., Stahl, A., & Fülöp, T. (2015). Radiation reaction induced non-monotonic features in runaway electron distributions. *Journal of Plasma Physics*, *81*, 475810502. https://doi.org/10.1017/S0022377815000513/

Hollmann, E. M., Aleynikov, P. B., Fülöp, T., Humphreys, D. A., Izzo, V. A., Lehnen, M., Lukash, V. E., Papp, G., Pautasso, G., Saint-Laurent, F., & Snipes, J. A. (2014). Status of research toward the ITER disruption mitigation system. *Physics of Plasmas*, *22*(2), 021802. https://doi.org/10.1063/1.4901251

Hoppe, M. (2024). DREAM documentation. https://ft.nephy.chalmers.se/dream/

Hoppe, M. (2021). *Runaway-electron model development and validation in tokamaks* [PhD thesis]. Chalmers University of Technology. https://research.chalmers.se/publication/527630

Hoppe, M., Embreus, O., & Fülöp, T. (2021). DREAM: A fluid-kinetic framework for tokamak disruption runaway electron simulations. *Computer Physics Communications*, *268*, 108098. https://doi.org/10.1016/j.cpc.2021.108098

Hu, D., Nardon, E., Hoelzl, M., Wieschollek, F., Lehnen, M., Huijsmans, G., van Vugt, D. C., Kim, S.-H., contributors, J., & team, J. (2021). Radiation asymmetry and MHD destabilization during the thermal quench after impurity shattered pellet injection. *Nuclear Fusion*, *61*(2), 026015. https://doi.org/10.1088/1741-4326/abcbcb

ITER. (2023). The ITER Tokamak. https://www.iter.org/mach

Koslowski, H. R. (2012). Operational limits and limiting instabilities in tokamak machines. *Fusion Science and Technology*, *61*(2T), 96–103. https://doi.org/10.13182/FST12-A13496

Lehnen, M., Aleynikova, K., Aleynikov, P., Campbell, D., Drewelow, P., Eidietis, N., Gasparyan, Y., Granetz, R., Gribov, Y., Hartmann, N., Hollmann, E., Izzo, V., Jachmich, S., Kim, S.-H., Kočan, M., Koslowski, H., Kovalenko, D., Kruezi, U., Loarte, A., . . . de Vries, P. (2015). Disruptions in ITER and strategies for their control and mitigation. *Journal of Nuclear Materials*, *463*, 39–48. https://doi.org/https://doi.org/10.1016/j.jnucmat.2014.10.075

Martín-Solís, J., Loarte, A., & Lehnen, M. (2017). Formation and termination of runaway beams in ITER disruptions. *Nuclear Fusion*, *57*(6), 066025. https://doi.org/10.1088/1741-4326/aa6939

Merriam-Webster. (2024). Tokamak. https://www.merriam-webster.com/dictionary/tokamak

Nardon, E., Hu, D., Artola, F. J., Bonfiglio, D., Hoelzl, M., Boboc, A., Carvalho, P., Gerasimov, S., Huijsmans, G., Mitterauer, V., Schwarz, N., Sun, H., the JOREK team, & contributors, J. (2021). Thermal quench and current profile relaxation dynamics in massive-material-injection-triggered tokamak disruptions. *Plasma Physics and Controlled Fusion*, *63*(11), 115006. https://doi.org/10.1088/1361-6587/ac234b

Nardon, E., Hu, D., Hoelzl, M., Bonfiglio, D., & the JOREK team. (2020). Fast plasma dilution in ITER with pure deuterium shattered pellet injection. *Nuclear Fusion*, *60*(12), 126040. https://doi.org/10.1088/1741-4326/abb749

OpenADAS. (2024). OPEN-ADAS. https://open.adas.ac.uk/

Pusztai, I., Ekmark, I., Bergström, H., Halldestam, P., Jansson, P., Hoppe, M., Vallhagen, O., & Fülöp, T. (2023). Bayesian optimization of massive material injection for disruption mitigation in tokamaks. *Journal of Plasma Physics*, *89*, 905890204. https://doi.org/10.1017/S0022377823000193

Pusztai, I., Hoppe, M., & Vallhagen, O. (2022). Runaway dynamics in tokamak disruptions with current relaxation. *Journal of Plasma Physics*, *88*, 905880409. https://doi.org/10.1017/S0022377822000733

Rechester, A. B., & Rosenbluth, M. N. (1978). Electron heat transport in a tokamak with destroyed magnetic surfaces. *Phys. Rev. Lett.*, *40*, 38–41. https://doi.org/10.1103/PhysRevLett.40.38

Reiter, D. (2000). The data file AMJUEL: Additional atomic and molecular data for EIRENE.

Reux, C., Plyusnin, V., Alper, B., Alves, D., Bazylev, B., Belonohy, E., Boboc, A., Brezinsek, S., Coffey, I., Decker, J., Drewelow, P., Devaux, S., de Vries, P., Fil, A., Gerasimov, S., Giacomelli, L., Jachmich, S., Khilkevitch, E., Kiptily, V., . . . JET contributors. (2015). Runaway electron beam generation and mitigation during disruptions at JET-ILW. *Nuclear Fusion*, *55*(9), 093013. https://doi.org/10.1088/0029-5515/55/9/093013

Rosenbluth, M., & Putvinski, S. (1997). Theory for avalanche of runaway electrons in tokamaks. *Nuclear Fusion*, *37*(10), 1355–1362. https://doi.org/10.1088/0029-5515/37/10/i03

Shiraki, D., Commaux, N., Baylor, L. R., Eidietis, N. W., Hollmann, E. M., Lasnier, C. J., & Moyer, R. A. (2016). Thermal quench mitigation and current quench control by injection of mixed species shattered pellets in DIII-D. *Physics of Plasmas*, *23*(6), 062516. https://doi.org/10.1063/1.4954389

Shultis, J., & Faw, R. (2002). *Fundamentals of nuclear science and engineering.* CRC Press.

Smith, Helander, P., Eriksson, L.-G., & Fülöp, T. (2005). Runaway electron generation in a cooling plasma. *Physics of Plasmas*, *12*(12), 122505. https://doi.org/10.1063/1.2148966

Smith & Verwichte. (2008). Hot tail runaway electron generation in tokamak disruptions. *Physics of Plasmas*, *15*(7), 072502.

Spitzer, L., & Härm, R. (1953). Transport phenomena in a completely ionized gas. *Phys. Rev.*, *89*, 977–981. https://doi.org/10.1103/PhysRev.89.977

Svenningsson, I., Embreus, O., Hoppe, M., Newton, S. L., & Fülöp, T. (2021). Hot-tail runaway seed landscape during the thermal quench in tokamaks. *Physical Review Letters*, *127*, 035001. https://doi.org/10.1103/PhysRevLett.127.035001

Vallhagen, O. (2023). *Disruption mitigation in tokamaks with massive material injection* [Licentiate thesis]. Chalmers University of Technology. https://research.chalmers.se/publication/535522

Vallhagen, O., Hanebring, L., Artola, J., Lehnen, M., Nardon, E., Fülöp, T., Hoppe, M., Newton, S., & Pusztai, I. (2024). Runaway electron dynamics in ITER disruptions with Shattered Pellet Injections.

Zeng, S., Zhu, P., & Ren, H. (2023). Species dependence of the impurity injection induced poloidal flow and magnetic island rotation in a tokamak. *Plasma Physics and Controlled Fusion*, *65*(12), 125001. https://doi.org/10.1088/1361-6587/ad02bc

DEPARTMENT OF PHYSICS
CHALMERS UNIVERSITY OF TECHNOLOGY
Gothenburg, Sweden
www.chalmers.se

CHALMERS
UNIVERSITY OF TECHNOLOGY